PERFORMANCE EVALUATION OF TWO CZT GAMMA RAY IMAGING SYSTEMS

A Thesis

Table of Contents

Acknowledgments iii

List of Tables vi

List of Figures vii

Abstract xii

1. Introduction 1
   1.1 Background on Gamma Cameras 2
   1.2 Motivation and Goals 3
   1.3 Outline of Thesis 5

2. Background 6
   2.1 CZT as a Radiation Detector 6
   2.2 Overview of LabRAT 10
      2.2.1 Detector Layout 10
      2.2.2 CZT Module Layout 11
      2.2.3 System Electronics: Internal Boards and DAQ Boards 13
      2.2.4 Collimator and Shielding 16

3. LabRAT Acquisition Software 17
   3.1 Initialization 19
   3.2 Acquisition ..... 206 Tc 0.7494 T

6. Discussion and Conclusions 65
6.1 Miswired Pixels 65
6.2 Discussion of NEMA Performance Test Results 66
6.2.1 Count Rate 66
6.2.2 Energy Resolution and Uniformity of Detector Response 67
6.2.3 Extrinsic Resolution 68
6.2.4 Linearity 71
6.2.5 Integral and Differential Uniformity 72
6.3 Future Work 72

References 75

Appendix A: Spatial Resolution Software 78

Appendix B: LabRAT Block Diagrams 81

Appendix C: Detector Initialization Parameters 84

Vita .....a12 506.44797 506.76073 Tm(8Tk Diagram)Tj12 0 0 12 27

List of Tables

1. Voltage offset values for LS Bias shift 30

2. Effect of LS Bias setting on the center channel of an ASIC's composite photopeak for LabRAT 1. A Tc-99m point source was used to produce the energy spectra..... 30

3. Summary of effect of LS Bias settings on the photopeak center channel for LabRAT 1. A Tc-99m source was used..... 31

4. Measured energy resolutions for LabRAT 0 before and after implementing the LS bias shifts..... 34

5. Curve fitting and energy resolution data for each module in both LabRAT systems..... 47

6. Measured values for average FWHM of the capillary tube images for horizontal and vertical orientations..... 55

7. Average fitted location of the slits in pixel coordinates for linearity tests using a slit phantom in vertical and horizontal orientations for both LabRAT systems..... 59

8. Integral and differential extrinsic uniformity values for the LabRAT systems for the entire detector FOV and for a smaller FOV that excludes a 1-pixel wide perimeter of edge pixels. The intrinsic uniformities, measured from a Tc-99m point source flood image used for detector tuning (Chapter 4) are shown for comparison..... 64

List of Figures

1. Photograph of LabRAT version 0 detector 1

2. Photograph of LabRAT version 1 detector 1

3. Illustration of side view of pixellated (left) and monolithic crystal (right) configurations for CZT detectors 7

4. Energy spectrum for a Tc-99m (140 keV photopeak) point source showing a shift of counts to the low energy side of the photopeak 9

5. Inside view of the electronics box of LabRAT 1 showing power supplies and signal processing boards 11

6. Photograph of an Imarad CZT module 12

7. Layout and connection of pixels in an Imarad CZT detector module. Each smaller box represents an individual pixel; the bold line marks the dividing line between ASICs 12

8. Photograph of the carrier board used in the LabRAT systems. The carrier board holds up to twenty-five CZT modules 15

9. Illustration of the carrier board layout. The orientation of ASICs is shown for module 1 and is the same for all modules. Control signals are daisy chained serially from one module to the next as demonstrated by the sequence of arrows 15

10. Three communications boards reside in the electronics box with the power supplies: the data processing board (left), the communications board (piggyback on left) and a passive signal adapter board (right) 16

11. Front panel for the LabRAT system software. Image display is shown in the inset 18

12. Front panel for the DFE initialization VI 20

13. Part of a LabRAT configuration file 20

14. Front panel for the MAKEDFEDEFAULTS program 21

15. EVENTS2DISK acquisition subprogram front panel 23

16. Image display VI showing a flood field acquisition for the LabRAT 1. Black squares are pixels that were disabled in the initalization VI..... 24

17. Sample per-pixel energy spectra for LabRAT 1, acquired by flooding the system with 140 keV gamma rays from a point source at 1.5 m distance. The pixel coordinate is noted above each graph and the channel with the most counts is recorded on each spectrum..... 28

18.

29. Photograph of LabRAT 0 count rate setup. LabRAT 0 is on the far right. The tungsten source holder is on the far-left on the box. The copper plates have not yet been placed over the end of the holder..... 38

30. Count rate vs. activity for LabRAT 1. The curves are linear as expected at low activities, then saturate at 3300 counts per second. The 2-second, 5-second and 10-second loops indicate the frequency at which the detector updates the image display 40

31. Count rate vs. activity for LabRAT 0. The curves resemble those in Figure 29 for LabRAT 1, except the count rate saturates at 3100 counts per second..... 40

32. Tungsten source holder and collimator discs used for spatial resolution and uniformity of response measurements 44

33. Point source scanning system with detector frame and point source holder. LabRAT 0 is in place on the frame 44

34. Energy spectrum obtained for a single pixel measured with the scanning source setup. Blue dots show measured data, red line shows the Gaussian plus exponential curve 45

35. Energy spectrum for the same pixel as in Figure 33, calculated with different initial input parameters to the curve fitting routine. The measured data are blue dots, the red line is the fitted function..... 45

36. Representative sample of pixel spectra from module 2 of LabRAT 0 for which the Gaussian plus exponential curve fitting routine produced an adequate fit using automated input parameters. Blue dots are measured data; the red line is the fitted function..... 46

37. Two dimensional bar plots of per-pixel FWHM energy resolution for LabRAT 1 (left) and LabRAT 0 (right)..... 47

38. Uniformity profile along the y-direction at x = 37 for LabRAT 1. Dips in the curve near 40 mm and 80 mm show the 1.2 mm gap between modules. Dips at the beginning and end are where the source was beyond the edges of the detector. Three individual pixel response profiles are shown for reference (see Figure 40). Each ASIC in a module contributes to about half of the width of that module's profile 50

39. Uniformity profile along the y-direction at x = 39 for LabRAT 0. The dip in the curve near 40 mm shows the 1.2 mm gap between modules. Three individual pixel response curves are shown for reference (see Figure 41)..... 51

40. Detail of detector response curve and three individual pixel profiles for LabRAT 1. The responses of adjacent pixels overlap because of charge-sharing between pixels. The overall detector response is the sum of all individual pixel responses 51

41. Detail of detector response curve and three individual pixel profiles for LabRAT 0. The responses of adjacent pixels overlap because of charge-sharing between pixels. The overall detector response is the sum of all individual pixel responses 52

42. Total counts acquired in all pixels as a function of motor position for LabRAT 1. The zero position is the center of a pixel; the twelve surfaces span a range representing two full pixels 52

43. Total counts acquired in all pixels as a function of motor position for LabRAT 0. The zero position is the center of a pixel; the twelve surfaces span a range representing two full pixels 53

44. Photograph of experimental setup for measuring extrinsic spatial resolution. The capillary tube is positioned parallel to and 5 cm above the collimator face. Lead sheet around the collimator provides lateral shielding 53

45. Photograph of the low-energy, all-purpose collimator used for extrinsic spatial resolution and uniformity measurements. This piece of collimator is a lead-foil, hexagonal hole design from a Siemens' LEAP collimator 54

46. Image of a 1 mm diameter capillary tube at 5 cm distance oriented diagonally, acquired with LabRAT 0 54

47. Windowed and unwindowed capillary tube images from LabRAT 1. Horizontal over module 2 is the orientation of the capillary tube relative to the Horizontal over m

windows must be applied on a per-pixel basis. Spatial uniformity is worse than for typical scintillator-based gamma cameras, while extrinsic spatial resolution is satisfactory.

Chapter 1

Introduction

The focus of this research is the performa

cad

1.1 Background on Gamma Cameras

Gamma cameras are used in nuclear medicine to provide functional imaging of patients. The patient is g

1.2 Motivation and Goals

The motivation for this work is to measure the imaging characteristics of the LabRAT systems. The detector hardware was designed and built by Mosaic Imaging Technology, Inc., with collaboration by my advisor, Dr. Matthews. Some rudimentary software had also been written. A performance evaluation had never been done for these systems. LabRAT 1 uses an updated version of some of the detector electronics whereas LabRAT 0 uses an older version of these same components. It is expected that the energy resolution, uniformity of detector

B. Identify NEMA performance standards relevant to monolithic crystal, position sensitive CZT systems such as LabRAT.

C. Acquire and evaluate performance data.

The programming required writing image acquisition software to produce real-time images and implementing the ability to use up to 25 CZT detector modules in one system (a detector module consists of a monolithic CZT crystal, the pins to attach it to a carrier board and the electronics necessary to process radiation interaction events). It was also necessary to develop a graphical user interface and update existi

4. Linearity.
5. Flood field uniformity.

1.3 Outline of Thesis

Chapter 2 gives background information on CZT as a detector material and describes the structural and functional details of the LabRAT systems. In Chapter 3 an overview is given of the programming for the LabRAT systems. Chapter 4 discusses the need to tune the detector and the method for doing so. The details about the methods, materials and results for the performance evaluation are given in Chapter 5. The discussion, conclusion and future work are discussed in Chapter 6.

radiation interaction events that occur within a given pixel will be counted toward that pixel only. In contrast, in a monolithic crystal with pixellation due to multiple contacts on the crystal, radiation interaction events near a contact will most likely be counted towards the pixel that is defined for that contact, but events near the borders between pixels that are not directly under a given contact can result in charge being shared by more than one pixel.

The good energy resolution in CZT is a result of a large numbers of charge carrriers being produced per electron-volt of energy deposited in the material and of a low Fano factor [5]. The Fano factor is the ratio of the variance of the number of electrons actually produced to the Poisson statistical expected

Some problems with CZT that lead to increased energy resolution values are charge carrier trapping, depth of interaction effects and boundary effects due to pixelation [4]. These contribute to the phenomenon of tailing on the low energy side of the photopeak that occurs in semiconductor detectors. Figure 4 shows an energy spectrum from LabRAT for a Tc-99m point source that demonstrates the tailing phenomenon. Imperfections in the crystal lattice of the semiconductor material cause charge carriers to become trapped before they are collected at the anode. Sato *et al.* [11] found that full collection of charge carriers in CZT is limited by the combination of short lifetimes and low mobilities especially for holes. Incomplete charge collection shifts events into the photopeak tail.

According to Schlesinger, incoming events that fall in the center of a pixel will contribute to the photopeak, while those near the boundaries will contribute to the low-energy tail [4]. Kalinosky *et al.* demonstrated that these boundary effects are due to

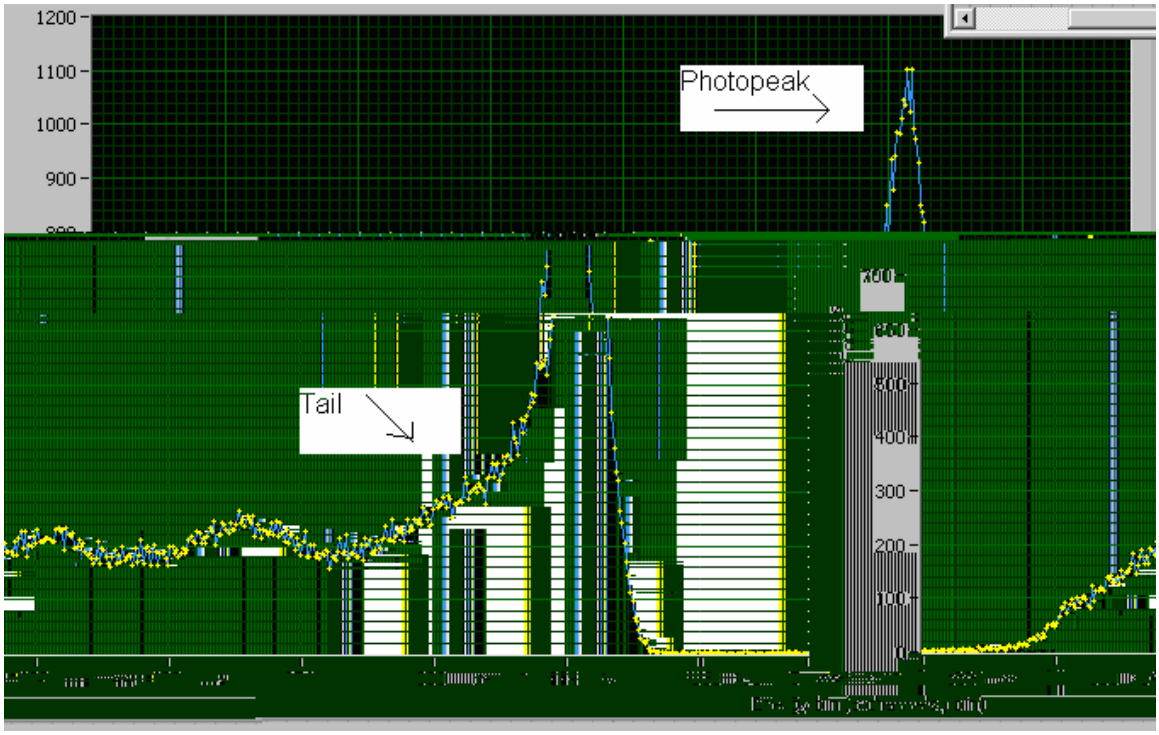

Figure 4. Energy spectrum for a Tc99m (140 keV photopeak) point source showing a shift of counts to the low energy side of the photopeak.

Currently, it is difficult to grow CZT crystals with perfect uniformity [6]. Imperfections may lead to charge trapping and problems with charge collection. Although Imarad (the manufacturer of the CZT modules used in the LabRAT systems) claims that “the volume of...a nuclear spectrometer can be made as large as one wishes, by assembling a multitude of modules” [15], at the current time the high cost of CZT detector modules (approximately $3000 per square inch for CZT crystals) restricts the uagng aystemus.

medical imaging. Work is being done on scintimammography detectors [20] using CZT and bone densitometers [21] are in use currently using CZT detectors, because both of these applications only require small fields of view. Other medical uses include miniature portable and intra-operative probes as well as detectors for cardiac imaging [22].

LabRAT is intended for use as an affordable, research-grade gamma radiation ray imaging system for small field of view applications. Uses include small animal imaging, portable radioisotope imaging in emergency room or intensive care units, and as an instruction tool for radiology residents and physics students.

2.2 Overview of LabRAT

2.2.1 Detector Layout

The LabRAT detector system hardware was built by Mosaic Imaging Technology, Inc. For LabRAT 1, detector modules and high voltage power supply are in one box and the electronics power supplies and the signal processing boards are in a separate box, as shown in Figure 5. The two boxes are connected by a ribbon cable for the data signals and a power cable to provide power from the electronics box to the detector box. The two boxes are made out of aluminum. The front plate is approximately 0.5mm thick where radiation events enter the detector.

A copper foil is mounted inside the front plate and electrically isolated from the box. The purpose of the foil is to distribute the high voltage over the cathode side of the detector modules. An aluminum framework within the box is used to hold heat sinks in

the detector box for LabRAT 1 are 31 cm x 31 cm x 27 cm. This is much larger than is actually necessary, to allow easy access to the detectors during development work.

In LabRAT 0, the power supplies are all external, while the detector modules and signal processing boards are located together in a single 31cm x 31 cm x 8 cm aluminum box. The box provides heat sinks for cooling and a copper foil for high voltage distribution.

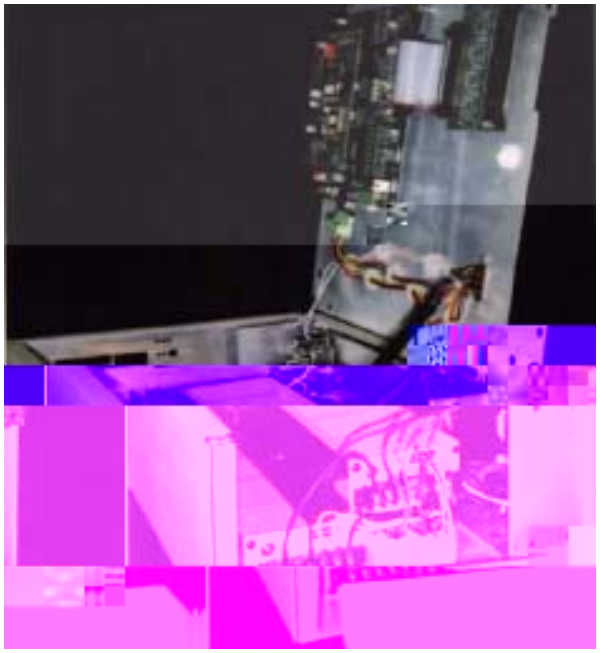

Figure 5. Inside view of the electronics box of LabRAT 1 showing power supplies and signal processing boards.

2.2.2 CZT Module Layout

Both versions of LabRAT contain CZT modules and components from Imarad, Ltd. [15]. Each CZT module is a 38.4 mm x 38.4 mm x 5 mm monolithic crystal divided into 16 x 16 pixels. Each pixel within the module is 2.4 mm x 2.4 mm x 5 mm. Figure 6 shows a CZT module like those used in the LabRAT systems. The pixel dimensions are determined by the size and layout of the contacts on the anode side of the crystal.

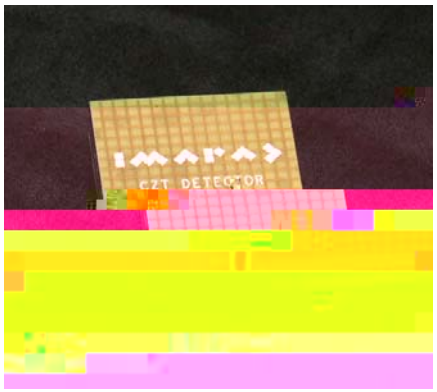

Figure 6. Photograph of an Imarad CZT module.

The pixels on each detector module are bonded to a pair of ASICs (application specific integrated circuits) that provide pulse shaping and pixel identification. Each module has two ASICs and each ASIC processes the signals for 128 pixels. Figure 7 illustrates the layout of the pixels and ASICs within each module [10]; this pixel map transl

The CZT and the ASICs are mounted on a circuit board that routes power, control signals and data signals in and out of the detector module. The circuit board pin-out mates to an industry standard microprocessor socket. When purchased from Imarad, each preassembled module comprised the CZT, the ASICs and the circuit board. The ASICs in the LabRAT systems were manufactured for Im

testing, LabRAT 0 originally had 3 modules in a column, but one module is no longer functioning. The LabRAT 1 was supposed to have four modules in a 2 x 2 array; one of

computer memory for processing into images by the acquisition software. The software is discussed in Chapter 3. The two acquisition computers being used with the LabRAT systems are Pentium-4e two acqui

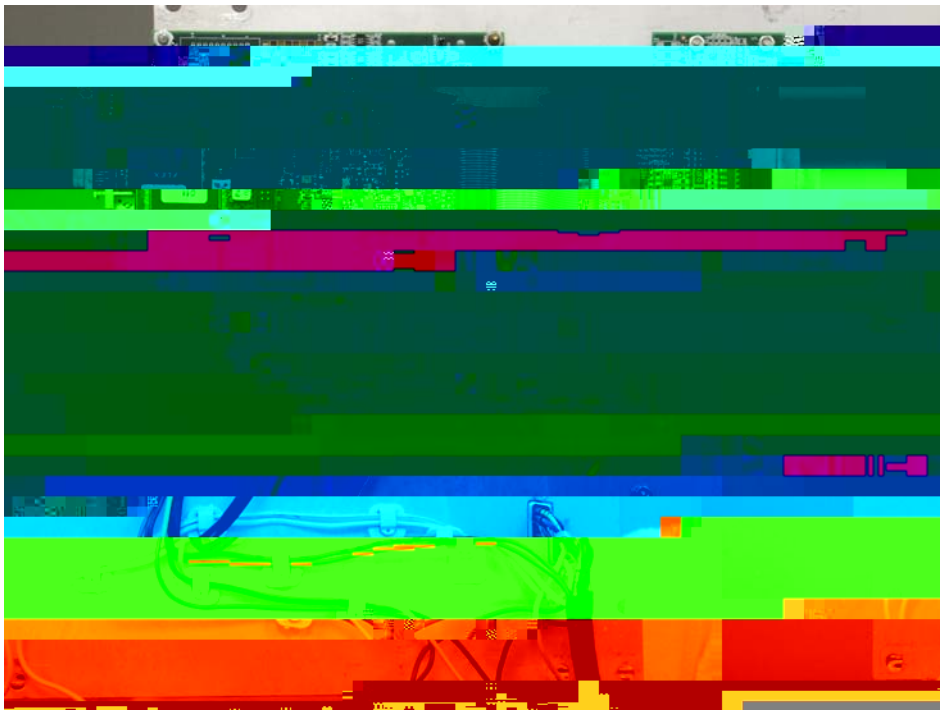

Figure 10. Three communications boards reside in the electronics box with the power supplies: the data processing board (left), the communications board (piggyback on left), and a passive signal adapter board (right).

2.2.4 Collimator and Shielding

The current LabRAT systems do not have dedicated collimators and shielding. For the purposes of minimizing design costs at the prototype stage, design of the collimator assembly has been deferred to future work. For this thesis, performance measurements requiring a collimator and shielding have been made using a piece of general-purpose, low-energy collimator and sheets of lead. These measurements are discussed in Chapter 5.

Chapter 3

individual pixel thresholds. All other parameters from the defaults file can be adjusted by the controls in this subVI as well.

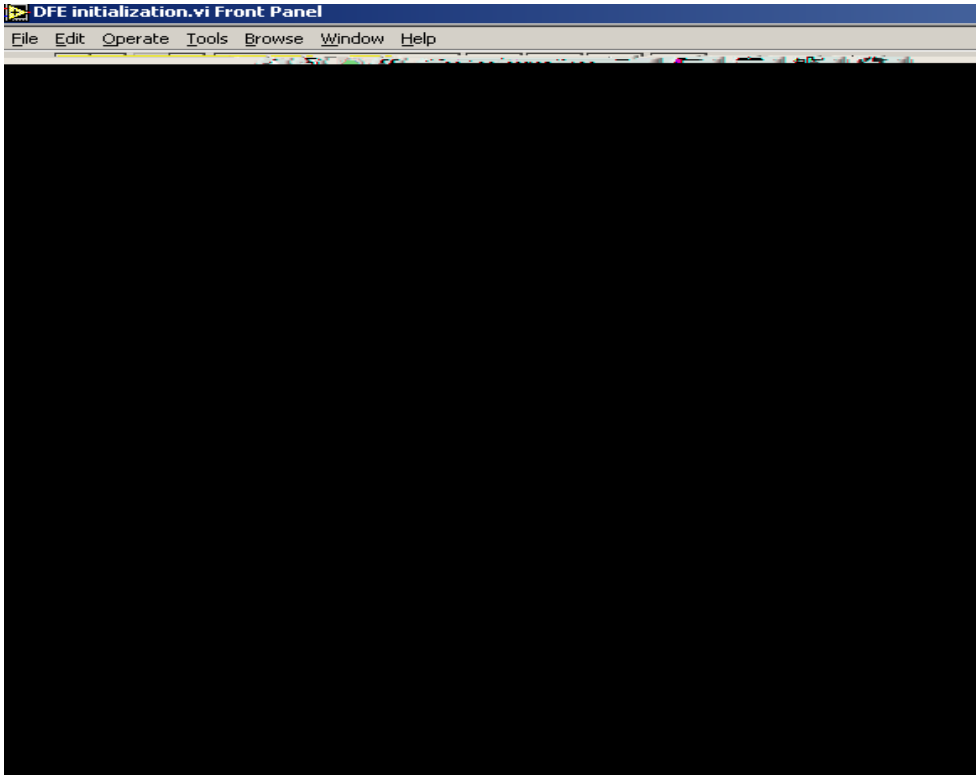

Figure 12. Front panel for the DFE initialization VI.

```
XaimDefaults3b.DFE
[DfeSettings]
PileupReject=TRUE
DfeThreshold=30.000000
[ASIC24]
Version=3.2
BlockLateTriggers=TRUE
DisableCurrentCompensation=FALSE
DisablePixels=0000000000000000000010000010001000000010000000000000000000000
0000000000000000000000000000000000000000000000000000000000000000000000000
AsicThreshold=0
PixelThresholds=0330000000000000000000000000000000000000000000000000000000
0000000000000000000000000000000000000000000000000000000000000000000000000
MainBias=0
TriggerWidth=0
TriggerDelay=0
ShapingTime=0
PreampFeedback=0
AnalogOutVref=1
TrimDAC=0
```

Figure 13. Part of a LabRAT configuration file.

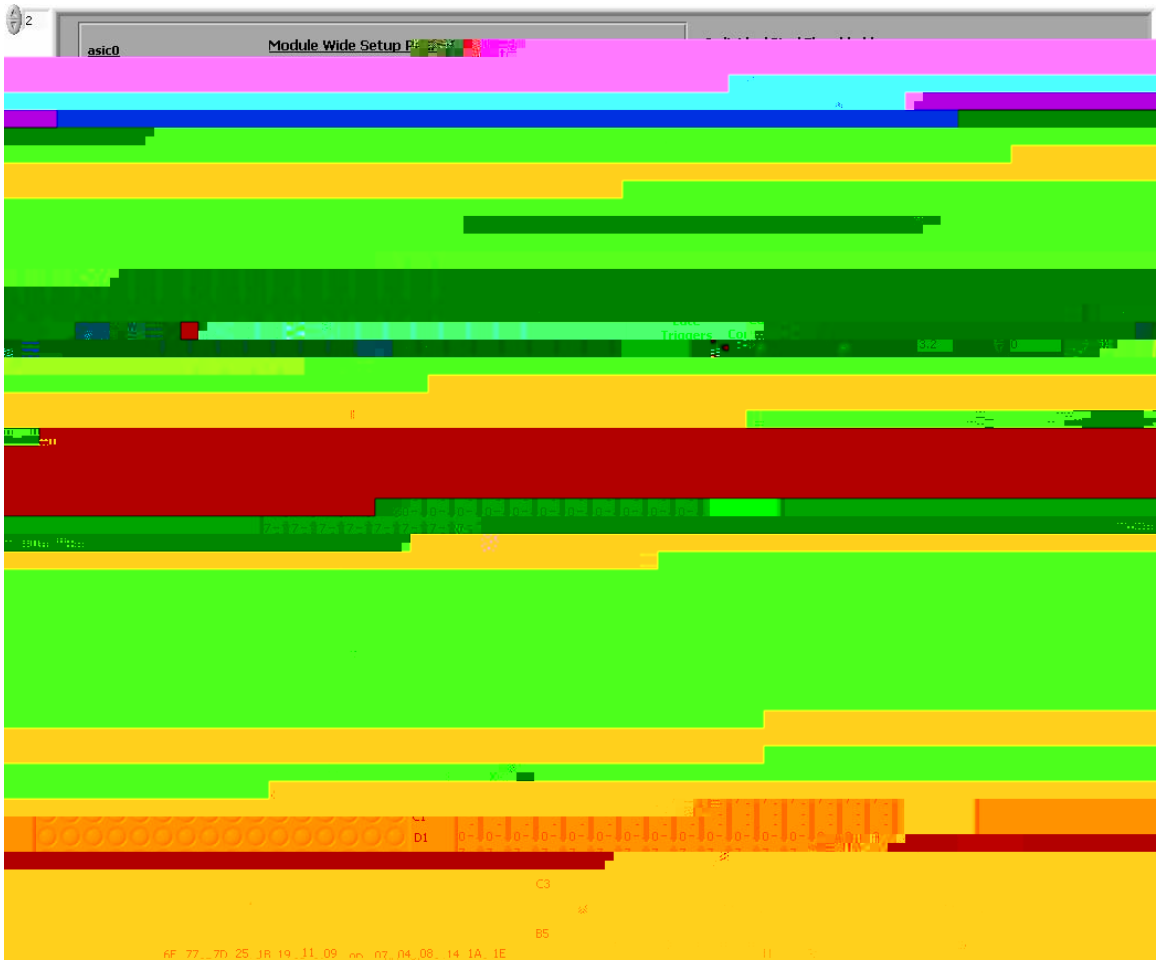

Figure 14. Front panel for the MAKEDFEDEFAULTS program.

3.2 Acquisition

Mosaic Imaging provided a rudimentary data acquisition program, but we rewrote essentially all parts of it. During acquisition, incoming photons 8188.196

EVENTS2DISK is comparable to that provided by Mosaic Imaging, we added the capability for the program to update the image display and energy spectra during the acquisition and to increase the acquisition speed of the software.

Each radiation interaction event from the detector that is sent to the computer contains two pieces of information: a pixel word encoding the location of the interaction in the detector and an energy word containing the energy information for that event. During acquisition, the two words are read from the detector, then the energy and pixel values are histogrammed into the energy spectrum and image. This histogramming includes checking the energy word to make sure that it is within the energy window and that no errors occured during the acquisition. Each pixel word comprises a seven bit value to specify the pixel within the ASIC, one bit to specify the ASIC within a module, and up to eight additional bits to specify the module within the detector system. The pixel map (see Figure 7) uniquely identifies each pixel in a module. Each module is uniquely identified by its location in the 5 x 5 matrix of detector modules according to the numbering scheme shown in Figure 9. Using the pixel map and module ID, each interaction location is mapped to its (x,y) coordinate for image display.

3.3 Image and Energy Spectra Display

The image and energy spectra display are fairly straightforward once the position and energy outputs have been decoded. The image display front panel is shown in Figure 16; the block diagram is shown in Appendix B. The image display contains a representative square for each pixel in each module of the detector. The total number of photon interactions in each pixel is represented with a color intensity relative to the number of interactions in other pixels. The maximum value of the color scale is mapped

Figure 16. Image display VI showing a flood field acquisition for LabRAT 1. Black squares are pixels that were disabled in the initialization VI.

Chapter 4

Tuning the Detector

Due to the pixelated structure of the detector and inherent inhomogeneities resulting from the fabrication process of the CZT crystals, there can be significant variation in the responses of individual pixels to identical signals. This was apparent immediately after we started obtaining en

photopeak center individually for each pixel. The measured photopeak centers can then be used during imaging to implement per pixel energy windows. These measurements are described in further detail in section 5.2. The ASIC design allows a baseline shift to be applied to all pixel outputs for an ASIC. This initialization parameter, called LS Bias, alters the baseline output voltage positively or negatively based on the value given to LS Bias in the ASIC initialization [10]. Table 1 gives the allowed LS Bias values. LS Bias provides a coarse adjustment to bring the photopeak center channel values into closer agreement.

We set a detector-wide gross threshold that seemed on average to remove the low end electronic noise without cutting off the signal. Then we measured the ASIC baseline voltage offset individually by running flood field acquisitions with a single ASIC turned on and seeing how the composite photopeak channel center changed as we adjusted the baseline voltage offset. The default setting was zero for all ASICs and voltage can be increased positively or negatively from the baseline which is zero volts.

We chose channel 350 for the desired photopeak channel location and adjusted the LS Bias on each ASIC to move its center channel closer to channel 350. Channel 350 was chosen by visually scanning the flood field pixel spectra (such as in Figures 16 and 17) for that ASIC and determining an approximate average for the channel number where the photopeak was occuring.

To complicate matters, the ASICs do not respond uniformly to the choice of LS Bias. For an identical change in LS Bias one ASIC might shift 25 channels while another would shift 40 or more. Table 2 summarizes the effect of LS Bias settings on the

ASICs of LabRAT 1. The pixel response was uniform enough for LabRAT 0 that we only changed the LS bias on one ASIC (ASIC 1 on module 3) by a shift value of one.

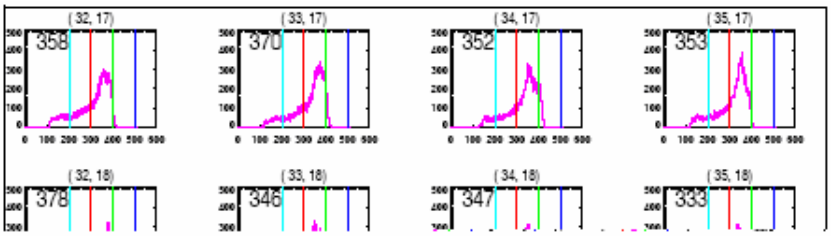

Figure 17. Sample per-pixel energy spectra for LabRAT 1, acquired by flooding the system with 140 keV gamma rays from a point source at 1.5 m distance. The pixel coordinate is noted above each graph and the channel with the most counts is recorded on each spectrum.

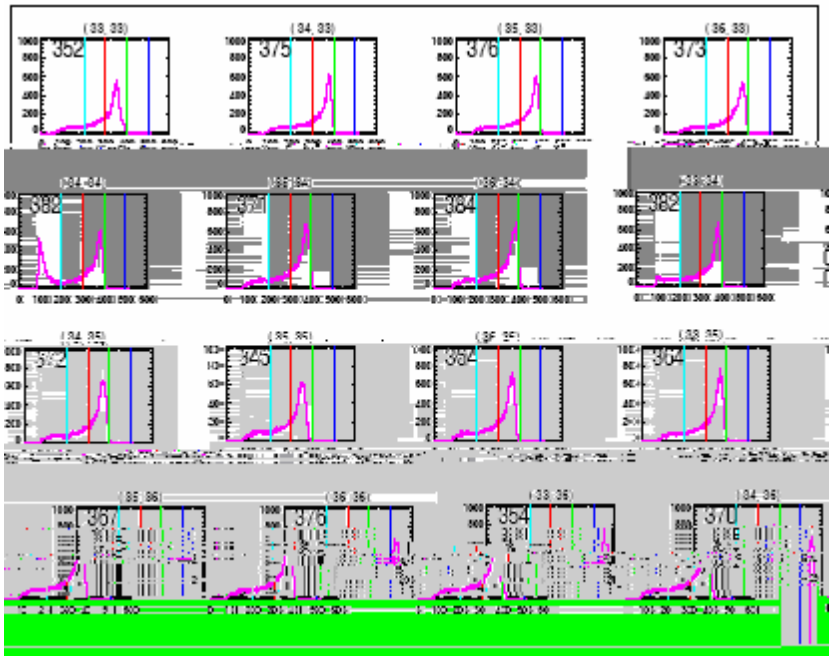

Figure 18. Sample per-pixel energy spectra for LabRAT 0, same measurement conditions as Figure 17.

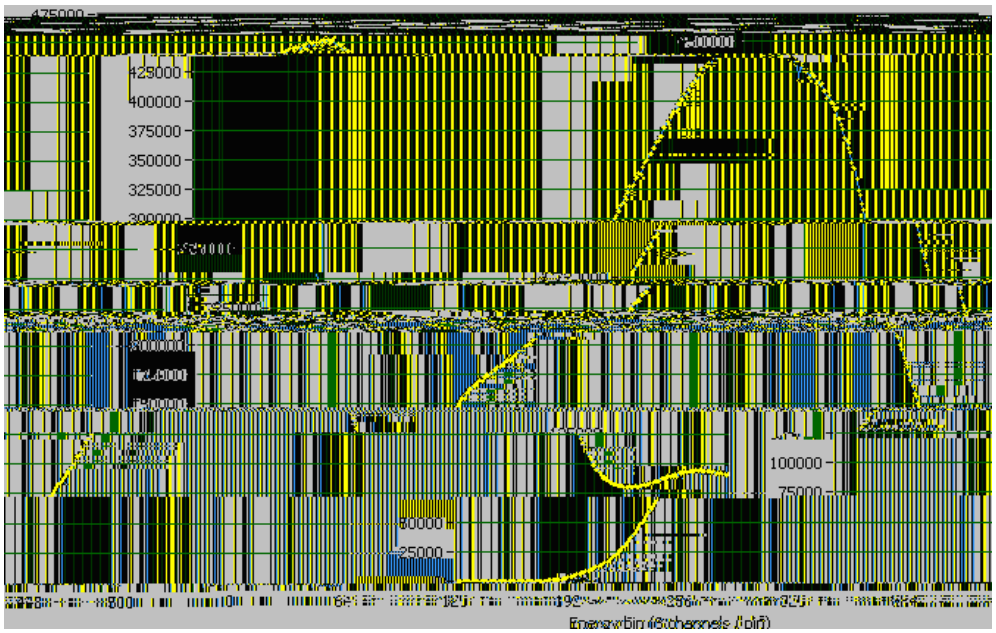

Figure 19. Composite energy spectrum for LabRAT 1, measured with a Tc-99m point source at 1.5 m distance. The spectrum contains ten million counts, default settings were used for all ASIC

Table 1. Voltage offset values for LS Bias shift.

Shift Value	Offset change (mV)
0	None

We collected flood field energy spectra before the LS Bias changes were implemented and then compared it to energy spectra taken after the changes were made. A Tc-99m source was used and ten million counts were gathered over the entire detector. Table 3 shows the results of the LS Bias changes. The average photopeak channel was calculated from the energy spectra for individual pixels, using the highest- count channel number (i.e., the channels noted on each spectrum in Figures 17 and 18). Figure 21 is the composite energy spectrum for LabRAT 1 acquired after the LS Bias shifts were implemented. The energy resolution according to this spectrum improved from 60% to 40% (compare to Figure 18).

Table 3. Summary of effect of LS Bias settings on the photopeak center channel numbers for LabRAT 1. A Tc-99m source was used.

	Peak Channel Numbers		
	Module 1	**Module 1**	**Module 1**
	ASIC 0	**ASIC 1**	**Module Average**
Default LS Bias Settings	**	**	288
New LS Bias Settings	346 +/- 119	325 +/- 113	336 +/- 116

Module 2

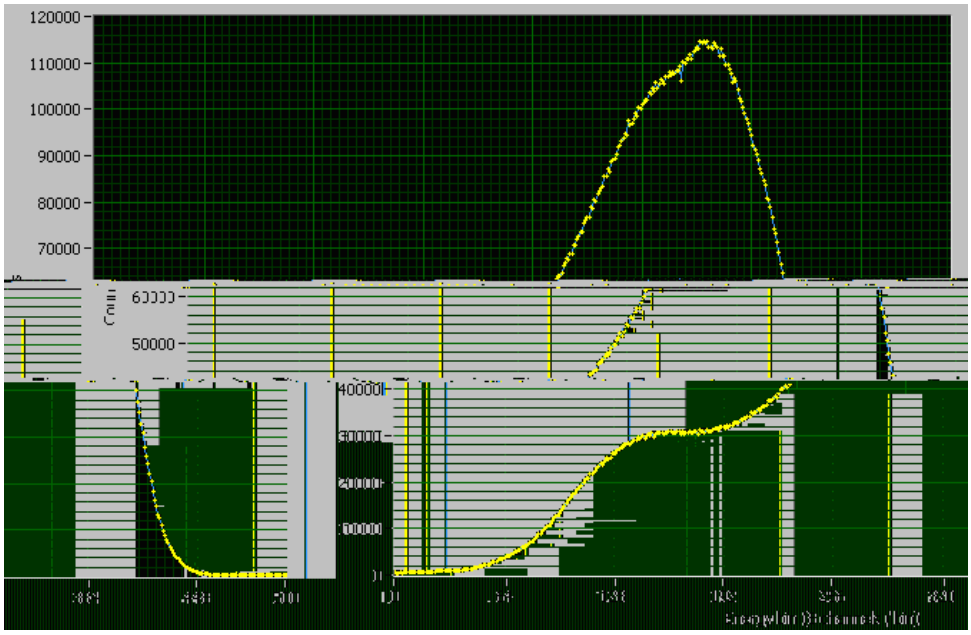

Figure 21. Composite energy spectrum for LabRAT 1 after the LS Bias shifts were implemented. Tc-99m was used as the flood source.

The effect of the LS Bias change for LabRAT 0 is less pronounced than for LabRAT 1, but still apparent. Figure 22 shows flood-field energy spectra from LabRAT 0 for a Ba-133 source before (left) and after (right) changing the LS Bias settings. Figure 23 shows flood-field energy spectra from LabRAT 0 for a Co-57 source before (left) and after (right) changing the LS Bias settings. Table 4 summarizes the effect of the LS Bias shifts on composite energy resolution for LabRAT 0. The effects of tuning are obviously critical for CZT detectors. The ability to apply baseline shifts to individual pixels is highly desirable, but unfortunately is not available with these ASIC designs.

For both LabRAT systems, the peak channel numbers were obtained from composite energy spectra using Tc-99m (140 keV photopeak), Co-57 (122 keV primary photopeak) and Ba-133 (81 keV primary photopeak) sources. Using these values and the known photopeak energies for these radionuclides, an energy calibration curve was

calculated for each system (see Figures 24 and 25). The three data points were fit to a straight line using Microsoft Excel. During imaging, the calibration curve can be used to display energy spectra in terms of keV rather than the more arbitrary value of channel numbers. Because the same software is operating both systems, with slightly different calibration curves, we have typically continued displaying energy spectra in terms of channels

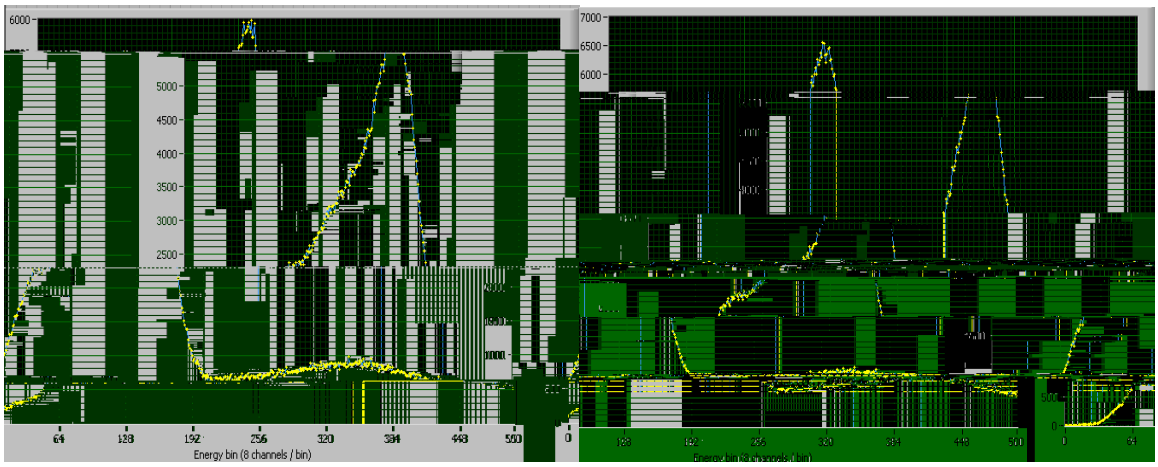

Figure 22. Composite energy spectra for LabRAT 0 with all LS Bias settings at zero (left) and with modified settings (right). The LS Bias of ASIC 1 on module 3 was the only setting changed. A Ba-133 source was used and one million total events were collected.

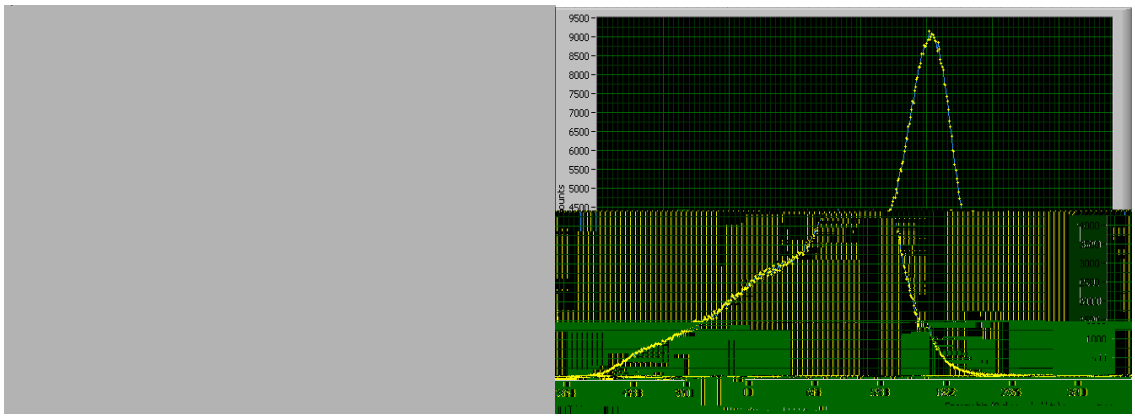

Figure 23. Composite energy spectra for LabRAT 0 with all LS Bias settings at zero (left) and with modified settings (right). The LS Bias of ASIC 1 on module 3 was the only setting changed. A Co-57 source was used and one million total events we

Table 4. Measured energy resolutions for LabRAT 0 before and after implementing the LS bias shifts.

	Energy Resolution (%)	
Flood Source	**Default LS Bias Settings**	**Modified LS Bias Settings**
Ba-133		

Chapter 5

LabRAT Performance Evalua

5.1 Count Rate Performance

The primary radionuclide used for this test was Tc-99m; Ba-133 was also used for some count rate measurements. The Tc-99m was placed in a plugged syringe cap (see Figure 26) wrapped in gauze and wedged into the middle of the length of the holder so it would stay in place. An illustration of the source geometry is given in Figure 27 and pictures of the setups for both detectors are given in Figures 28 and 29. NEMA specifies that the distance between source and detector be at least 5 times the maximum dimension of the useful field of view (UFOV). On a scintillation crystal gamma camera, a margin around the outside edge of the crystal is not usable, so the UFOV is smaller than the detector dimensions. With CZT the entire surface of the module is part of the field of view (FOV). Some authors have noted a tendency for edge pixels to respond differently than other pixels. Wagenaar states that "pixels located on the edges and especially the corners of the square arrays generally are less responsive than internal pixels" [6]. In our measurements, we did not notice a distinct enough pattern of response to systematically correct for edge effects. The FOV for LabRAT 1 is 38.4 mm x 117.6 mm (38.4 mm for each of three modules plus 1.2 mm gaps between modules). The FOV for LabRAT 0 with its two modules is 38.4 mm x 78 mm. As long as the source-detector distance is at least 58.8 cm, the NEMA criterion is satisfied for both detectors. We used 100 cm and 150 cm distances for the count rate tests.

Ten-million and twenty-million count flood fields were acquired for the two systems; the energy and pixel locations of each interaction were saved in list-mode by the LabRAT acquisition software. Programs were written in IDL to read the data from the

file, sort it by pixel and construct an energy spectrum for each pixel. These data were used for tuning the detector, described in Chapter 4, and shown in part in Figures 17 and 18.

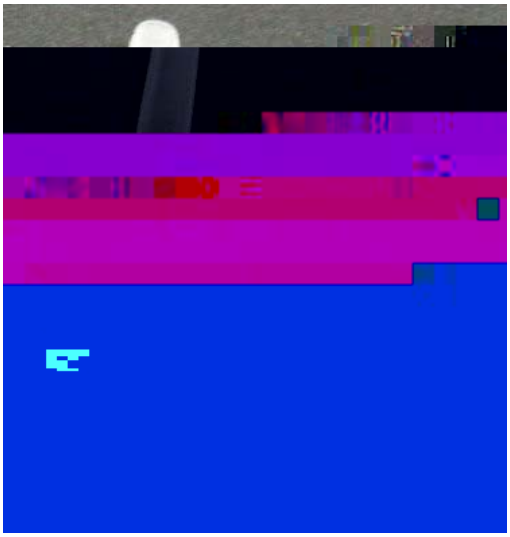

Figure 26. Syringe caps used to hold Tc-99m.

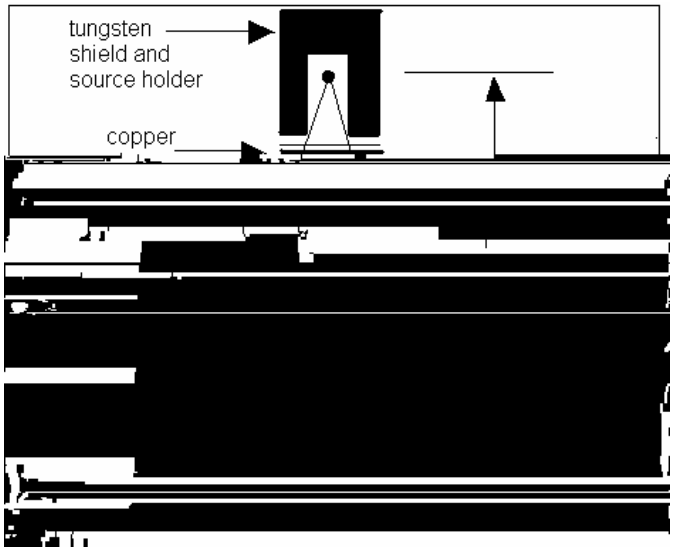

Figure 27. Source and detector geometry for count rate measurements.

Figure 28. Photograph of Labrat 1 count rate setup. LabRAT 1 is at the far left and the acquisition computer is in the background; the tungsten source holder is at the far right on the white block.

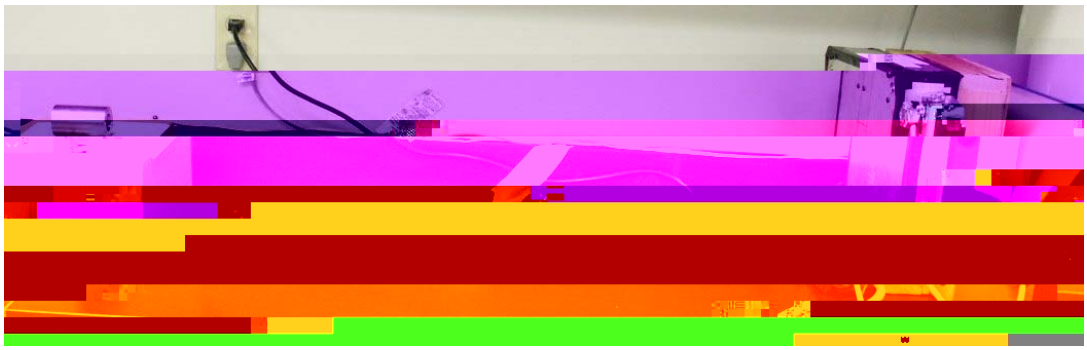

Figure 29. Photograph of LabRAT 0 count rate setup. LabRAT 0 is on the far-right. The tungsten source holder is on the far-left on the box. The copper plates have not yet been placed over the end of the holder.

The idea behind the count rate tests is to measure the "observed count rate for a 20% count loss and a maximum count rate" [3]. We started with 16.5 mCi of Tc-99m for one acquisition with LabRAT 1, with 2.34 mCi of Tc-99m for one acquisition with LabRAT 0, and with a 7.77 mCi Tc-99m source positioned equidistant between both detectors for yet another acquisition.

The count rate at the face of a LabRAT system from a Tc-99m source is given approximately by

$$C = A \cdot Y \cdot \Omega(a,d) \cdot \varepsilon(5\,mm, 140\,keV) \qquad (2)$$

where

C = count rate at detector (counts/sec)
A = source activity (disintegrations/sec)
Y = yield (0.89 gammas/disintegration)
$\Omega(a,d)$ = solid angle subtended by detector of area a at distance d
$\varepsilon(5\,mm, 140\,keV)$ = absorption efficiency of detector, ~88% for 5 mm of CZT at 140 keV

Thus,

$$C\,(cps) = A(mCi) \cdot 5.69 \times 10^{4}\ {}^{cps}\!/_{mCi} \qquad \text{(for 150 cm distance)} \qquad (3)$$

and

$$C\,(cps) = A(mCi) \cdot 1.28 \times 10^{5}\ {}^{cps}\!/_{mCi} \qquad \text{(for 100 cm distance)} \qquad (4)$$

For the 16.5 mCi source at 150 cm from the detector, the count rate should have started out at approximately 98,000 counts per second. For the 7.7 mCi source at 100 cm the count rate should have started around 103,000 counts per second.

Imarad's documentation obtained with the CZT modules indicates that the detector acquisition board (DAB) can process 1 million events per second [17]. The DAB converts current based detector outputs to voltage signals which are then stored in digital memory. Both of the detectors demonstrated a count rate maximum around 3300-3500 counts per second! Figures 30 and 31 show the count rate vs. activity for both detectors.

We could not obtain accurate measurements of the maximum count rate and 20% count loss from these measurements because of the abrupt saturation at 3300-3500 counts per second. Attempts were made to reconfigure the acquisition loops and to remove any extra tasks that might restrict the count rate; so far, none of these attempts have solved the problem.

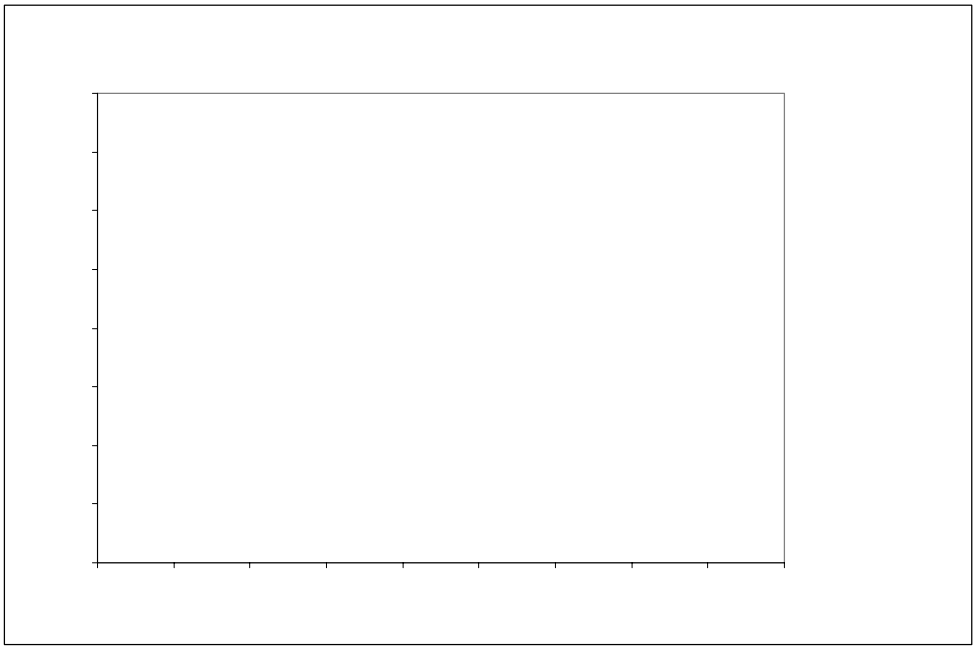

Using an 8 Ci Ba-133 source, a Tektronix TDS 5054 digital phosphour oscilloscope, an Ortec 551 timing single channel analyzer and an Ortec 871 timer/counter we measured the rate of trigger signals directly from the detector data cable. A background count rate reading from LabRAT 1 of 74 cps had been obtained using the LabRAT acquisition program. From the direct trigger signal measurements, a comparable background count rate of 70 cps was measured.

For the Ba-133 source an average count rate of 60,000 cps was measured from the trigger signals. This suggests that the detector hardware is capable of higher count rates than those measured with the LabRAT software and that the restricting factor has been narrowed down to the National Instruments acquisition cards and/or the L

For the spatial resolution and uniformity of response acquisitions we used a Velmex MaXY motorized translation stage with an NF90 motor controller [26]. The stage's stepper motors are capable of positioning the source holder with precision movement in steps as small as 0.005 mm across the (x,y) plane of the detector. We added a custom frame to the translation stage to hold the detector during the measurements. The frame, translation stage and LabRAT 0 are shown in Figure 33; the LabRAT system mounts "detector-down" over the translation stage and source holder.

A derivative version of the LabRAT software was created for use with the scanning stage; this augmented software integrates the translation stage drivers into the acquisition program. The output list-mode data format was modified to record the motor positions and acquisition start time, in addition to the energy and pixel location information. LabView VIs and a driver library were provided by Velmex with the NF90 motor controller.

5.2.1 Energy Resolution

To measure an accurate energy resolution value for each pixel, the source was stepped across the plane of the detector so that energy spectra were obtained at the center of each pixel for 15 seconds per pixel. The resulting data were decay corrected. To obtain the energy resolution measurements reported in Chapter 4, we measured the FWHM directly from the composite energy spectrum. This is not a feasible approach for per-pixel energy spectra because there is an exponential tail on the low energy side of the photopeak [4] (see Figure 4). A proposed method for measuring energy resolution for CZT energy spectra is to measure the half width at half maximum from the high-energy side of the photopeak and double the value to get the FWHM [27].

Narita et al. [19] recommend fitting the speing

energy resolution values. Figure 36 shows a representative sample of pixels that were suitable for automated curve fitting.

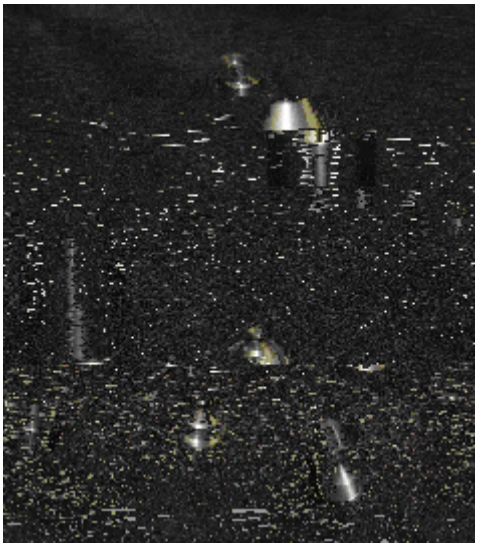

Figure 32. Tungsten source holder and collimator discs used for spatial resolution and uniformity of response measurements.

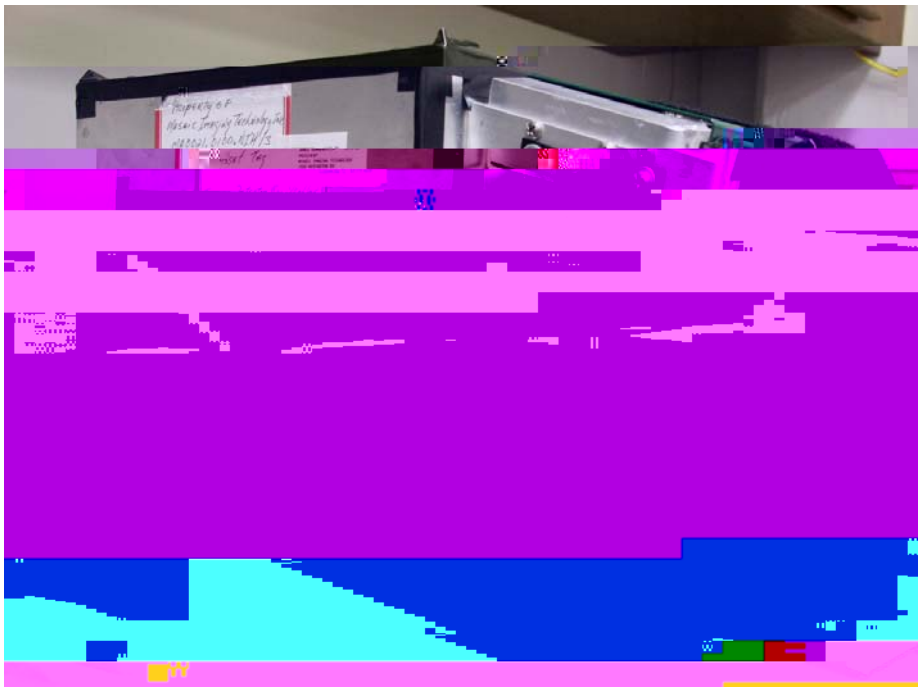

Figure 33. Point source scanning system with detector frame and point source holder. LabRAT 0 is in place on the frame.

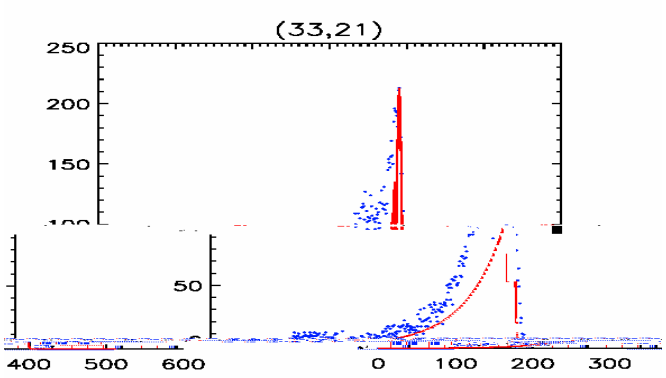

Figure 34. Energy spectrum obtained for a single pixel measured with the scanning source setup. Blue dots shows measured data, red line shows the Gaussian plus exponential curve.

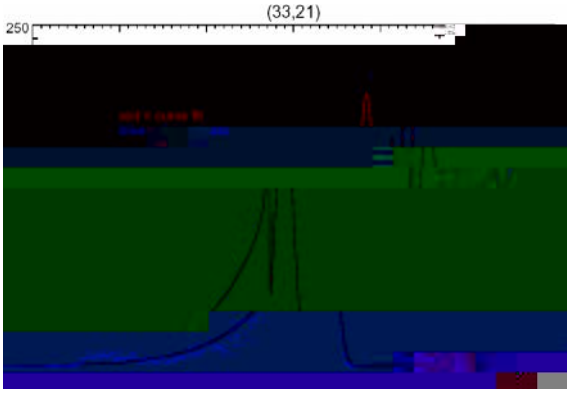

Figure 35. Energy spectrum for the same pixel as in Figure 33, calculated with different initial input parameters to the curve fitting routine. The measured data are blue dots, the red line is the fitted function.

For a handful of pixels, we ran the curve fit routine individually (the pixel in Figures 34 and 35 is such an example). Pixels with an automated energy resolution fit of less than 5% or greater than 10% were re-checked by hand. For some pixels, we were able to obtain a “better” fit by changing the input parameters; for others the data was so irregular (possibly due

Table 5 shows, for both LabRAT systems, the total number of pixels enabled in each module (the other pixels had been disabled during ASIC initialization because they were excessively noisy or dead), the total number of pixels that did not produce usable fits to the spectra, the total number of pixels that had to be analyzed individually and the average per-pixel energy resolution for each module. The overall average per-pixel energy resolution for LabRAT 0 is (7.0 +/- 2.51) % and for LabRAT 1 is (6.48 +/- 2.49)% (compare this to the composite energy resolutions of 27% and 40% respectively for LabRAT 0 and LabRAT 1 reported in Chapter 4). The percentage of pixels with an energy resolution less than or equal to 7% is 72.4% for LabRAT 1 and 58.7% for the LabRAT 0. Again, note that the energy resolutions are measured at 140 keV. Graphical plots of the per-pixel FWHM energy resolution as a function of (x,y) position in the detector are shown in Figure 37.

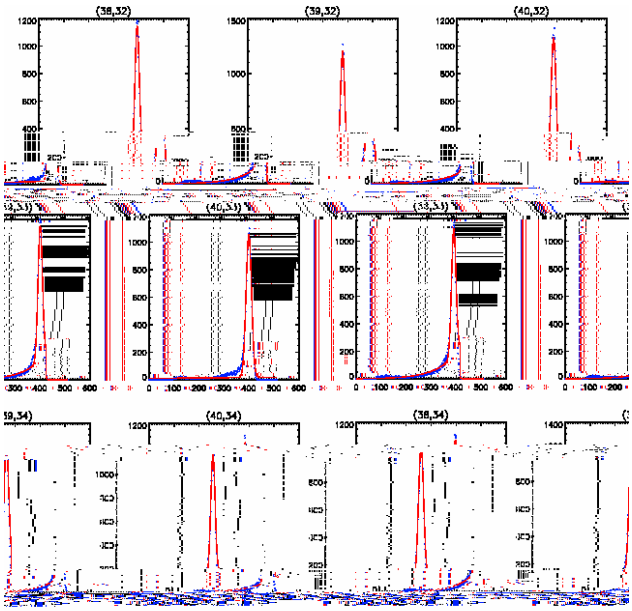

Figure 36. Representative sample of pixel spectra from module 2 of LabRAT 0 for which the Gaussian plus exponential curve fitting routine produced an adequate fit using automated input parameters. Blue dots are measured data; the red line is the fitted function.

an error in the ASIC layout in the pixel bonding pattern, or simply in the ASIC documentation, the events in each pixel of the pair are mis-assigned to the other pixel. Events and energy spectra for these pixels can be recovered if the pixel data are swapped in the software. This reduces the number of unfit pixels by four for each module. These miswired pixels are discussed further in Chapter 6.

5.2.2 Uniformity of Detector Response

For the uniformity of detector response measurements the source was stepped in 0.4 mm increments along a profile across the length of the detector (across all modules). Each measurement was acquired for fifteen seconds and the resulting data was decay corrected. The data was sorted to group the gamma interaction events that occured in each pixel as the source moved across the detector. Figures 38 and 39 show the response profiles for LabRAT 1 and LabRat 0. The uniformity of response is acceptable for both systems, with the expected dips in the profile at the gaps between modules; the 1.2 mm gap between modules is clearly seen in the profiles for both detectors. On the profile for LabRAT 0 there appear to be dips between the ASICs as well. The slight fluctuation in the response curve is likely due to the position dependent amount of charge sharing between pixels and inherent heterogeneity in charge trapping and collection efficiency.

Individual pixel responses for representative adjacent pixels are shown for the two LabRAT systems in Figures 40 and 41. These curves illustrate how the response of a pixel increases as the source steps into a pixel and reaches a maximum when the source is under the pixel center. The response then decreases as the source moves away from the center, reaching a minimum when the source is over the boundary between pixels. The overlap of the curves for the two pixels demonstrates the phenomenon of charge-sharing

setup is shown in Figure 44, the collimator is shown in Figure 45, and Figure 46 shows a sample image acquired for the diagonal orientation with LabRAT 0 with the windowed image on the left and the image without the energy window applied shown on the right.

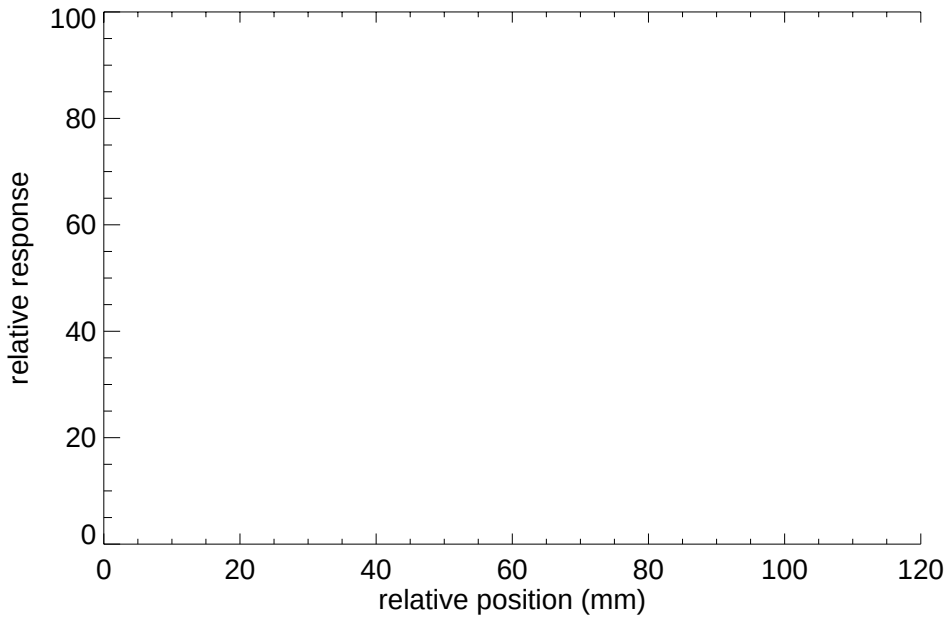

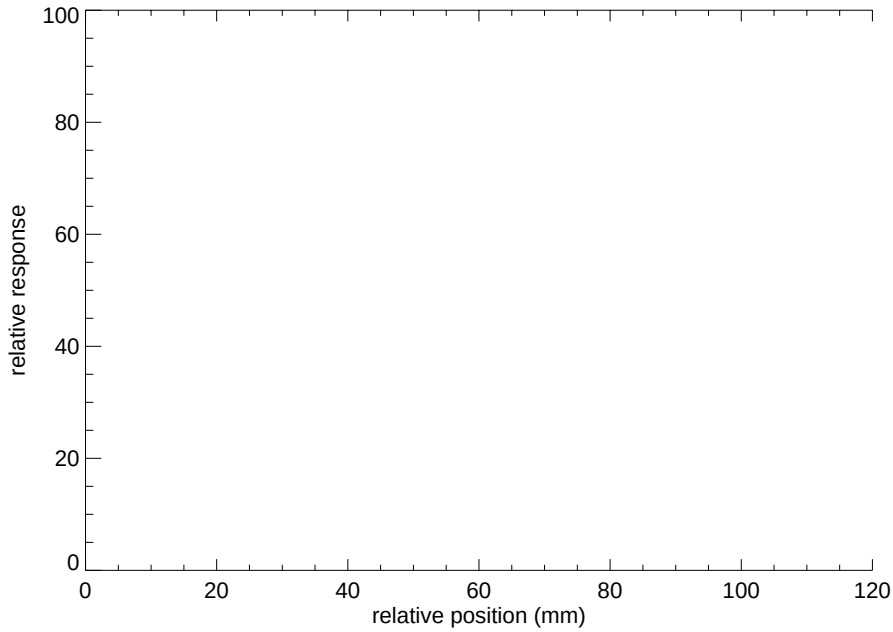
100
80
60
40
20
0
relative response
0
20
40
60
80
100
120
relative position (mm)

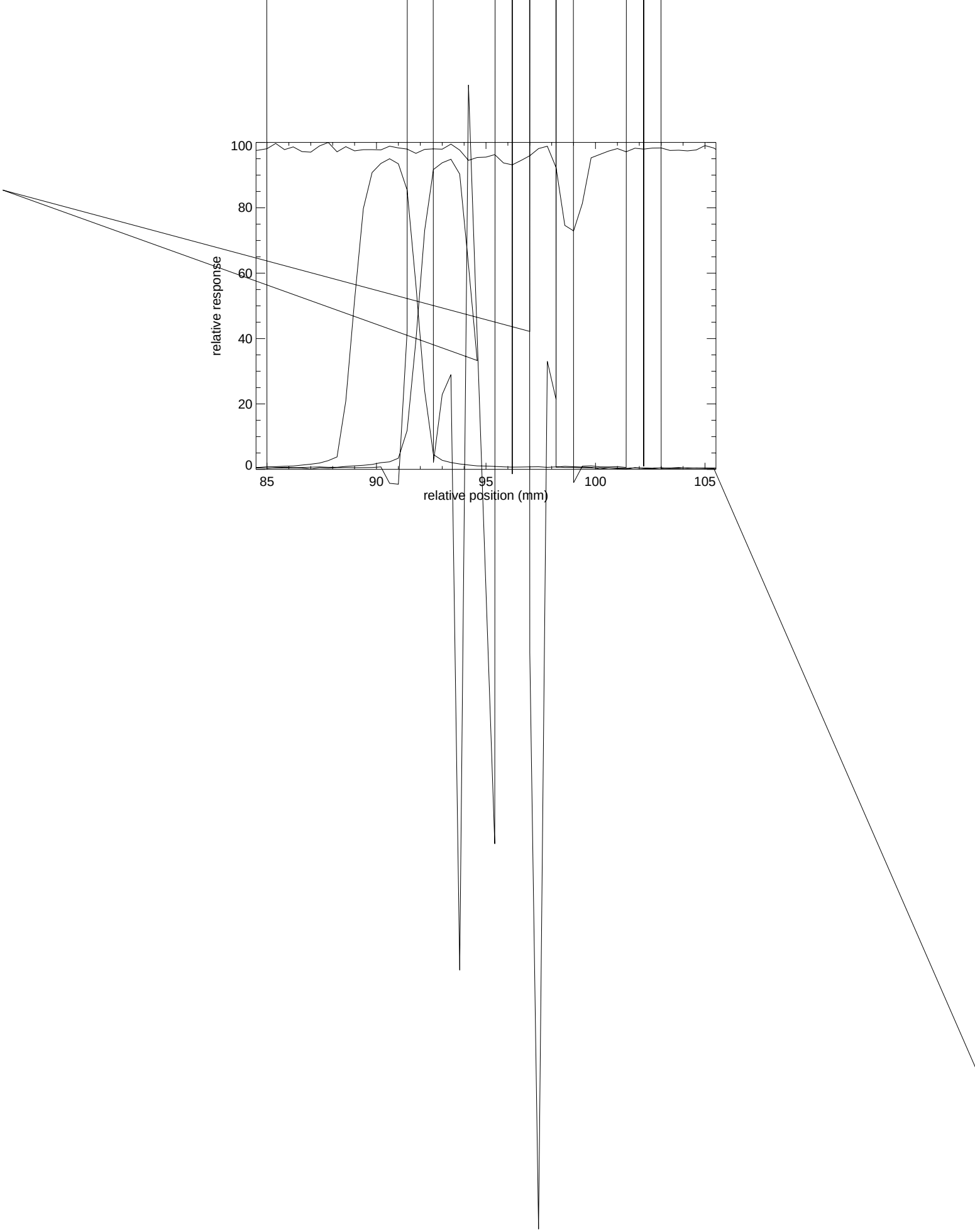
100
80
60
40
20
0
relative response
85
90
95
100
105
relative position (mm)

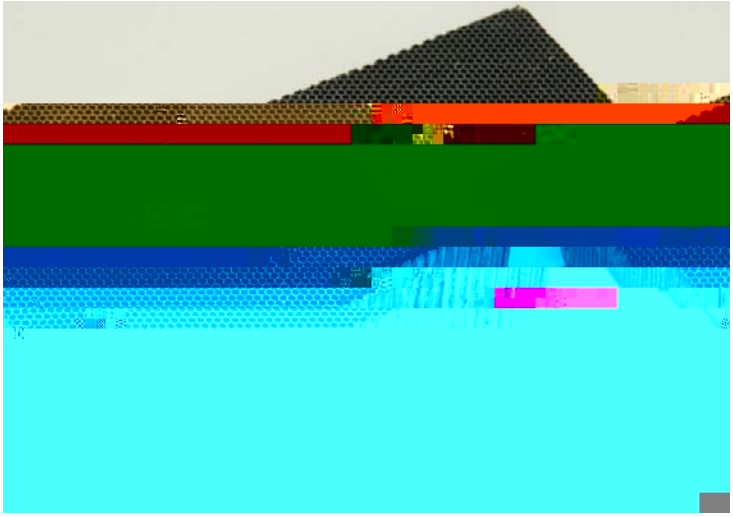

Figure 45. Photograph of the low-energy, all-purpose collimator used for

using the per-pixel fitted photopeak centers (parameter A_1 of equation 5) obtained from the energy resolution measurements of section 5.2.1. For the horizontal and vertical orientations, profiles of the pixels across the axis of the capillary tube were obtained. When dead pixels were present in the images, the average value of the eight pixels surrounding the dead pixel were used for the dead pixel. Each

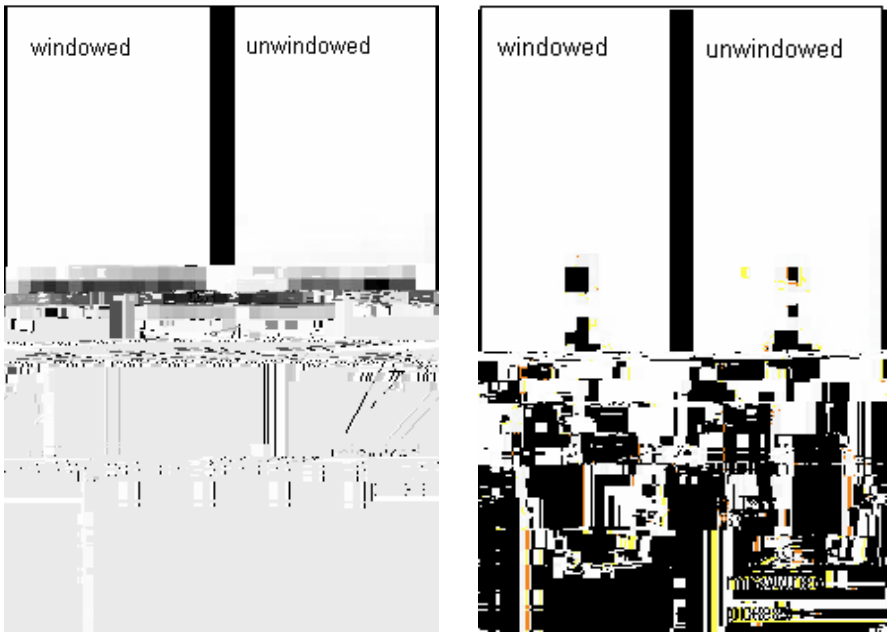

Figure 47. Windowed and unwindowed capillary tube images from LabRAT 1. Horizontal over module 2 is the orientation of the capillary tube relative to the detector for the two figures on the left, vertical over modules 2 and 3 is the orientation for the two on the right.

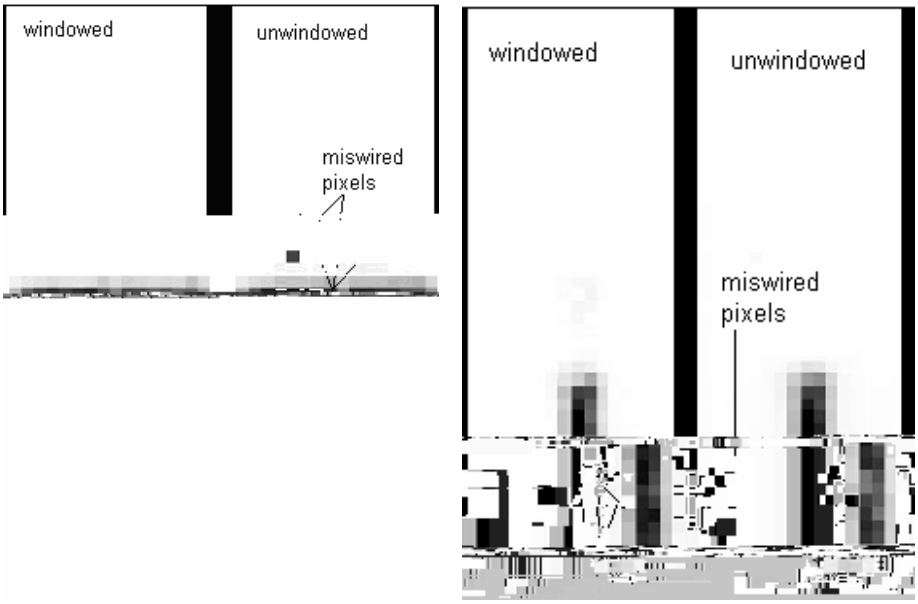

Figure 48. Windowed and unwindowed capillary tube images from LabRAT 0. Horizontal over module 2 is the orientation of the capillary tube relative to the detector for the two figures on the left, vertical over module 3 is the orientation for the two on the right.

5.4 Linearity

For these tests we used the same setup as the count rate measurements (section 5.1) but we placed a lead slit phantom against the detector face. Shown in Figure 49, the slit phantom is a 15 cm x 15 cm x 3.1 mm sheet of lead glued between 3.1 mm thick sheets of acrylic. Slits of 1 mm width spaced at 15 mm intervals are cut into the lead. The source was 2.3 mCi of Tc-99m placed at 100 cm distance from the detector. One million counts were acquired at each orientation (horizontally, vertically, diagonally) of the slit phantom.

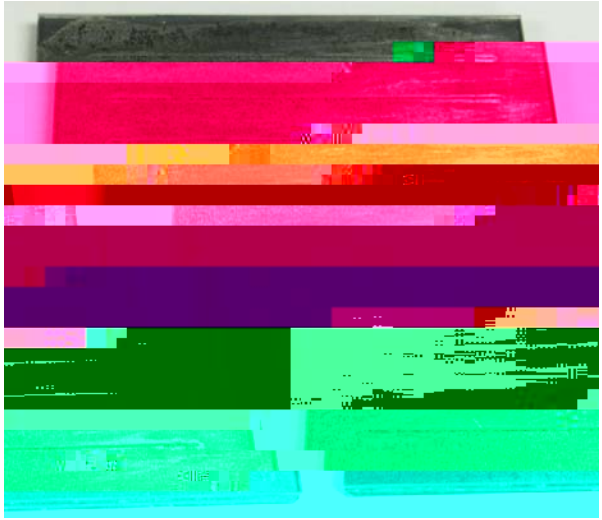

Figure 49. Slit phantom for linearity measurements.

For the linearity measurements it is expected that if the slits are aligned to the rows or columns of pixels and a slit is located above a row or column of pixels, the windowed image will be contained within that single row or column of pixels. It is also expected that if the source lines up along the border between two rows or columns of pixels, the events will share signals between the rows or columns; many of these events

will have energies that fall in the tails of the photopeak so that after energy windowing is applied, many of the counts in these rows or columns will be rejected from the image. Also, there is a 1.2 mm (or half-pixel wide) gap between modules. We expected that the image of a diagonal orientation of the slit phantom might show a discontinuity in the image where two modules meet, because our image does not account for the physical gap. However, the pixelation of the detector overwhelms any chance of seeing this discontinuity. Figure 50 shows an image of the diagonal orientation of the slit phantom from LabRAT 0.

Figure 50. Windowed and unwindowed slit phantom images from LabRAT 0, showing a diagonal orientation of the phantom relative to the detector.

Table 7 shows the average fitted center locations for the vertical and horizontal orientations for both detectors. The center locations were obtained by fitting a Gaussian function to profiles perpendicular to the slits. The fitted centers for all profiles of a slit were then averaged. Figures 51 and 52 show the images for each slit orientation for the

two LabRAT systems, with the unwindowed data on the right and the images with the energy window applied on the left.

Table 7. Average fitted location of the slits in pixel coordinates for linearity tests using slit phantom in vertical and horizontal orientations for both the LabRAT systems.

	Ave. Fitted Center of the Slit (Pixel Coordinate)
Columns Coordin	**Coordin**

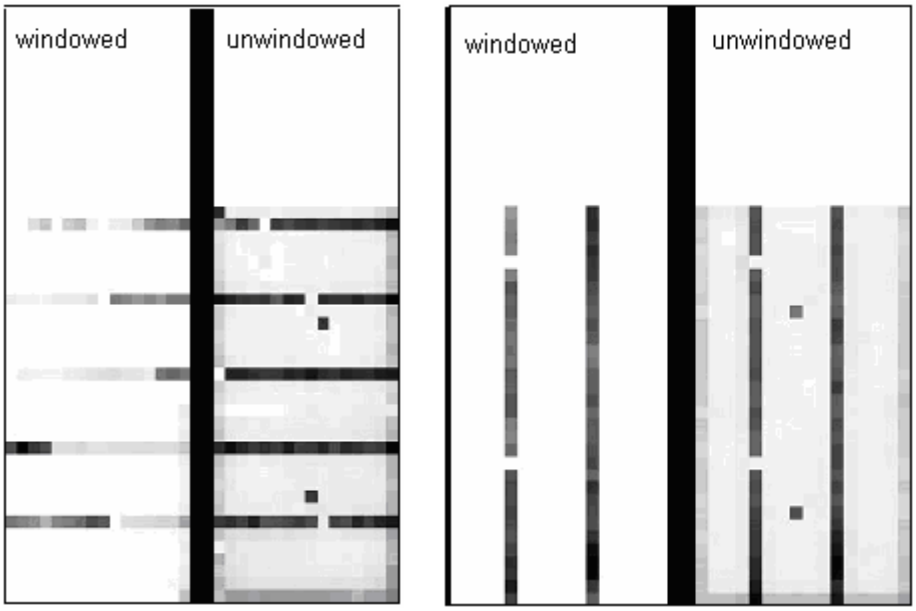

Figure 52. Slit phantom images from LabRAT 0. O 0. O

For the uniformity measurements we filled a 15 cm x 15 cm x 1 cm volume acrylic water tank phantom (see Figure 53) with 2.8 mCi of Tc-99m. We placed the collimator piece over the modules on the face of the detector, surrounded the collimator with lead shielding and placed the water phantom over the collimator. This collimator setup is identical to that used for the extrinsic spatial resolution measurements; the detector setup is shown in Figure 54. The raw image from LabRAT 0 is shown in Figure 55.

The image data is smoothed with a nine point filter function as recommended by NEMA, after dead pixels had been replaced with the averages of their neighbors. NEMA also specifies a 15% energy window on the flood-field uniformity image data. When we applied the 15% per-pixel energy window to our data, the resulting images became

8 9312.2 598.5609 Tm(easurem)Tj12.00.99985 405.36327T241.99312 59c5c7n(ity ij1PTjued with a nine)Tj

and bottom rows exhibited either no response (fully shielded by lead sheet) or extremely high response due to penetration between the collimator edge and the lead sheet. For the LabRAT 1 water tank data we calculated the uniformity values for the remaining rows of pixels as the full FOV and then rem

Table 8. Integral and differential extrinsic uniformity values for the LabRAT systems for the entire detector FOV and for a smaller FOV that excludes a 1-pixel wide perimeter of edge pixels. The intrinsic uniformities, measured from

Chapter 6

Discussion and Conclusions

This chapter summarizes the performance characterization results for the LabRAT systems. Section 6.1 discusses the issue of dead and miswired pixels in the detector modules. In section 6.2 the results of the performance tests are discussed. Future work on the LabRAT systems and general comments on the utility of CZT gamma cameras are discussed in section 6.3.

6.1 Miswired Pixels

We discovered in the course of our research that the same four pixels were consistently bad in each module. Figures 56 and 57 show an entire module's worth of pixel spectra for each system to demonstrate the location of these four pixels. These abnormal pixels were not detected during the analysis of overall detector data such as the flood field or count rate studies where large groups of pixels were measured at once; the pixels seemed to function normally. It was not until we began to compare individual pixel spectra that we discovered this pattern. These pixels are connected consecutively to the 42nd and 43rd input circuits in each ASIC [7]. Their hexadecimal pixel values according to the pixel map (Figure 7) are 2A and 2B in ASIC 0 and AA and AB in ASIC 1. With 128 pixels connected to each ASIC, AA and 2A correspond to the same pixel in sequence but on opposite ASICs, as do AB and 2B. It appears that the pairs of pixels are miswired, presumably by swapping the bonding order when the module was manufactured. A collimated source placed under pixel AA shows up in the image display

for pixel AB and vice versa; pixels 2A and 2B are similarly swapped. All four pixels appear to function in a reasonably normal way, aside from misplacing events in their partner pixels. Fortunately, the fix for this is straight forward. In the acquisition software, any events measured in one of the pixels are specifically reassigned to the other pixel. (In point of fact, the fix is actually just a matter of altering the numbering scheme of the pixel map. The original error could even have been typographical in the documentation rather than a manufacturing issue.) In any case, the issue is common to all of these modules and is particularly troublesome because it does not show up on routine flood images but could cause misinterpretation of patient images.

We discovered this late in the data analysis. Therefore, all of our data was acquired with this problem. For the extrinsic spatial resolution, integral and differential uniformity and linearity images we manually swapped the pairs of pixels in each image before performing the analysis. The pixel map has now been altered to exchange the pixel pairs, so future acquisi

at low activities (below the 3000-3500 cps saturation level) both detectors exhibit normal behavior (see Figures 29 and 30) and it is expected that if the count rate limitation is rem

The difference between the two detectors must be a result of the change in ASIC design; LabRAT 0 uses 3.0 version ASICs and LabRAT 1 uses 3.2 version ASICs. It is expected that near the boundaries between two pixels, charge sharing will reduce the counts in both of the pixels; near the center of a pixel most of the counts will contribute to that pixel. This expectation was confirmed in our research as demonstrated in Figures 42 and 43.

6.2.3 Extrinsic Resolution

A collimator is a necessary part of being able to accurately reconstruct position information in images obtained in nuclear medicine. Ideally and necessarily, a given detector system will be equipped with a collimator that conforms to the specifications of that system. The LabRAT systems currently do not have collimators designed specially for them, this is part of the future work to be done on this system. What was used as a collimator in these extrinsic resolution measurements was a piece of low-energy all-purpose parallel hole collimator. One source of error in this may include the fact that the collimator that we used had hexagonal holes and the LabRAT detector pixels are square. Another source of error comes from the fact that ideally the holes in the collimator would be aligned as precisely as possible to the pixels to prevent Moire patterns through interaction of the pixel and collimator lattices [27]. Ideally, the lead septa in the collimator would cover the boundaries between pixels, but such precision alignment was not possible for our study using an unmatched collimator.

The intrinsic resolution for these detectors is limited to the pixel size of 2.4 mm. The extrinsic resolution is a measurement of the intrinsic resolution for a detector combined with the collim

1. Improve tuning: whether it is possible for the manufacturer to improve the detector module ASICs to enable more precise fine tuning is not known to us, but such improvement

LabRAT systems would be improved by having greater control over tuning of individual pixels. The LabRAT systems had reasonable spatial resolution and per-pixel energy resolution, but overall energy resolution and uniformity were somewhat disappointing. In all, continued improvements of CZT detector systems are probably warranted and CZT gamma cameras will likely become a useful alternative to NaI(Tl) cameras for small FOV applications.

References

1. Matthews, K.L.II., Development and Application of a Small Gamma Camera. PhD.Thesis, The University of Chicago, 1997.

2. Shah, K.S., Glodo,J., Klugerman,M., Higgins,W., Gupta,T. and Wong,P. High Resolution Scintillation Spectrometers. Retrieved Feb 2005 from http://www.rmdinc.com/papers/HighEnergyResolutionScint.pdf

3. NEMA NU 1 Performance Measurements for Scintillation Cameras. 2001. Rosslyn,Va.

4. Schlesinger, T.E. and James, R.B. (eds). **Semiconductors for Room Temperature Nuclear Detector Applications.** Vol. 43. Academic Press, San Diego, 219-378, 1995.

5. Knoll, Glenn F. **Radiation Detection and Measurement 3rd edition.** John Wiley & Sons Inc., New York, 2000.

6. Wagenaar, D.J. CdTe and CdZnTe Semiconductor Detectors for Nuclear Medicine Imaging. In: **Emiss1 1 4415/ℓ¼phy The UFun**

11. Sato, G., Parsons, A., Hullinger, D., Suzuki, M., Takahashi, T., Tashiro, M., Nakazawa, K., Okada, Y., Takahashi, H., Watanadbe, S., Barthelmy, S., Cummings, J., Gehrels, N., Krimm, H., Markwardt, C., Tueller, J., Fenimore, E., Palmer, D. Development of a Spectral Model Based on Charge Transport for the Swift/Bat 32K CdZnTe Detector Array.. Preprint submitted to Elsevi

21. Vidal-Sitjes, G., Baldelli, P. and Gumbaccini, M. A CdZnTe Pixel Detector for Bone Densitometry. **Nucl. Inst. Methods in Phys. Res. A 518,** 401-403, 2004.

22. Scheiber, C. and Giakos, G.C. Medical Applications of CdTe and CdZnTe Detectors. **Nucl. Inst. Methods in Phys. Res. A 458**, 12-25, 2001.

23. --.National Instruments LabView. National Instruments Corp. Austin,TX. www.ni.com

24. --. IDL Research Systems Inc. Boulder,Co. www.rsinc.com/idl/

25. --. **Users Guide NF90 Series.** Velmex, Inc.Bloomfield,NY. www.velmex.com

26. Keyser, R.M. Characterization of Room Temperature Detectors using the proposed IEEE Standard. **IEEE Nucl. Sci. Symp. Med. Imag. Conf. Rec.** 2001.

27. Gunter, D.L, Matthews II, K.L. and Ordonez, C.E. The Interaction of Collimator Lattice Periodicity and Detector Pixellation. **Conference Record of the 1998 IEEE NSS/MIC,** paper M07-54, 1998.

28. Gunter, D.L. Collimator Design for Nuclear Medicine. In: **Emission Tomography, The Fundamentals of PET and SPECT.** Wernick, M.N. and Aarsvold, J.N. (eds). Elsevier Academic Press, San Diego, 153-168, 2004.

Appendix A

Spatial Resolution Software

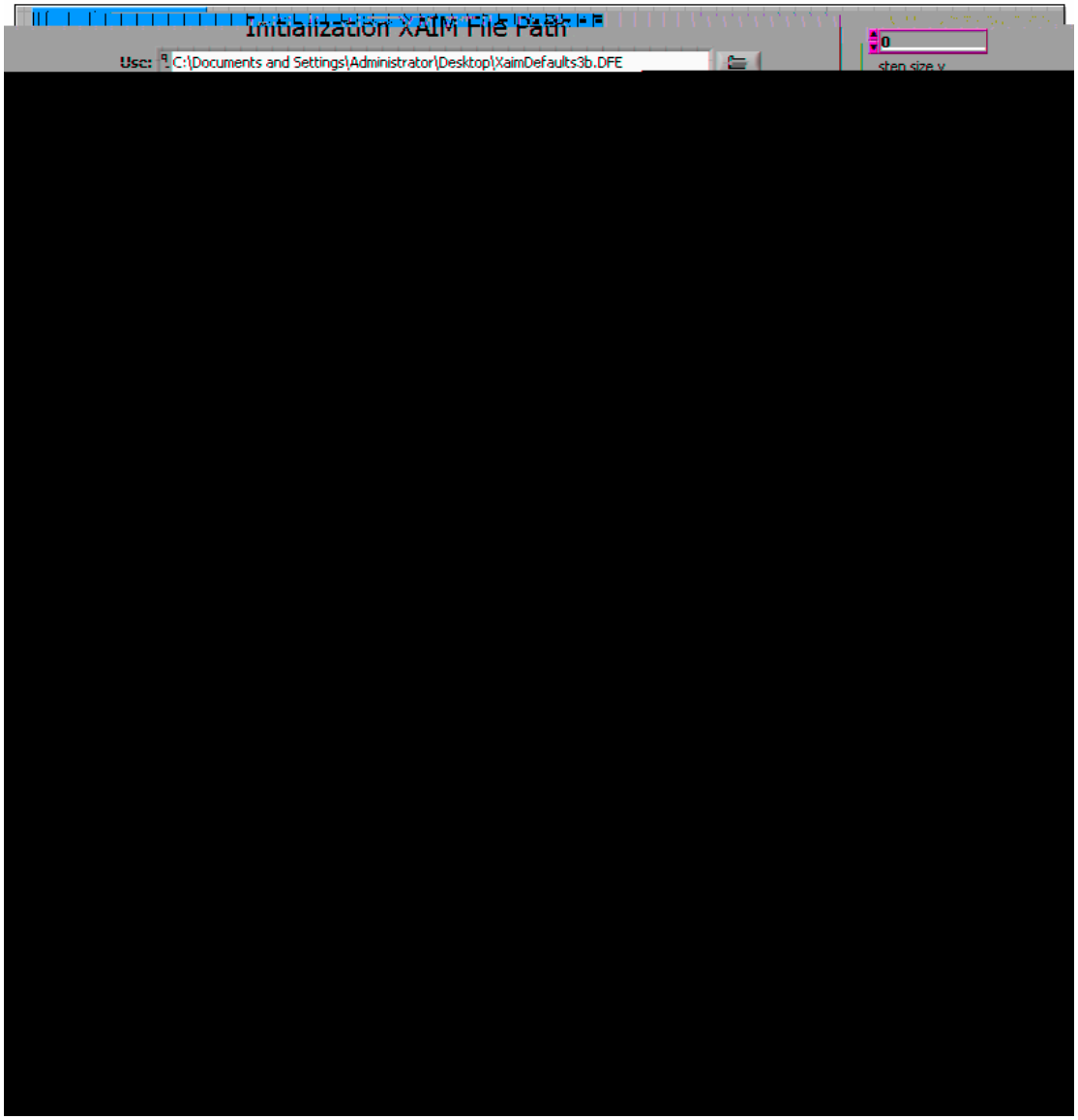

Figure A.1. User interface for spatial resolution version of system software. The main difference is the addition of controls to run the translation stage (seen

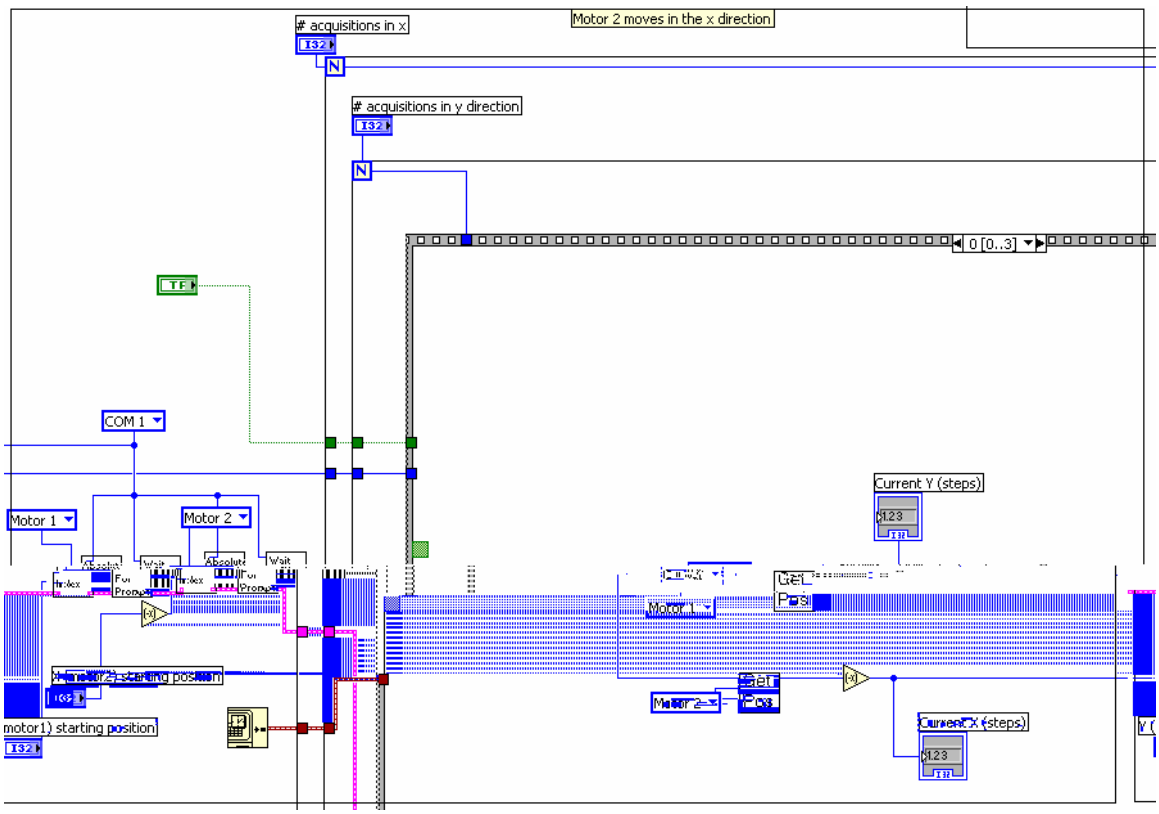

Figure A.2. Partial view of one loop of spatial resolution block diagram. Subprograms to initialize translation stage can be seen outside the loop to the left. The Get Pos boxes inside the loop get the current motor positions of the translation stage.

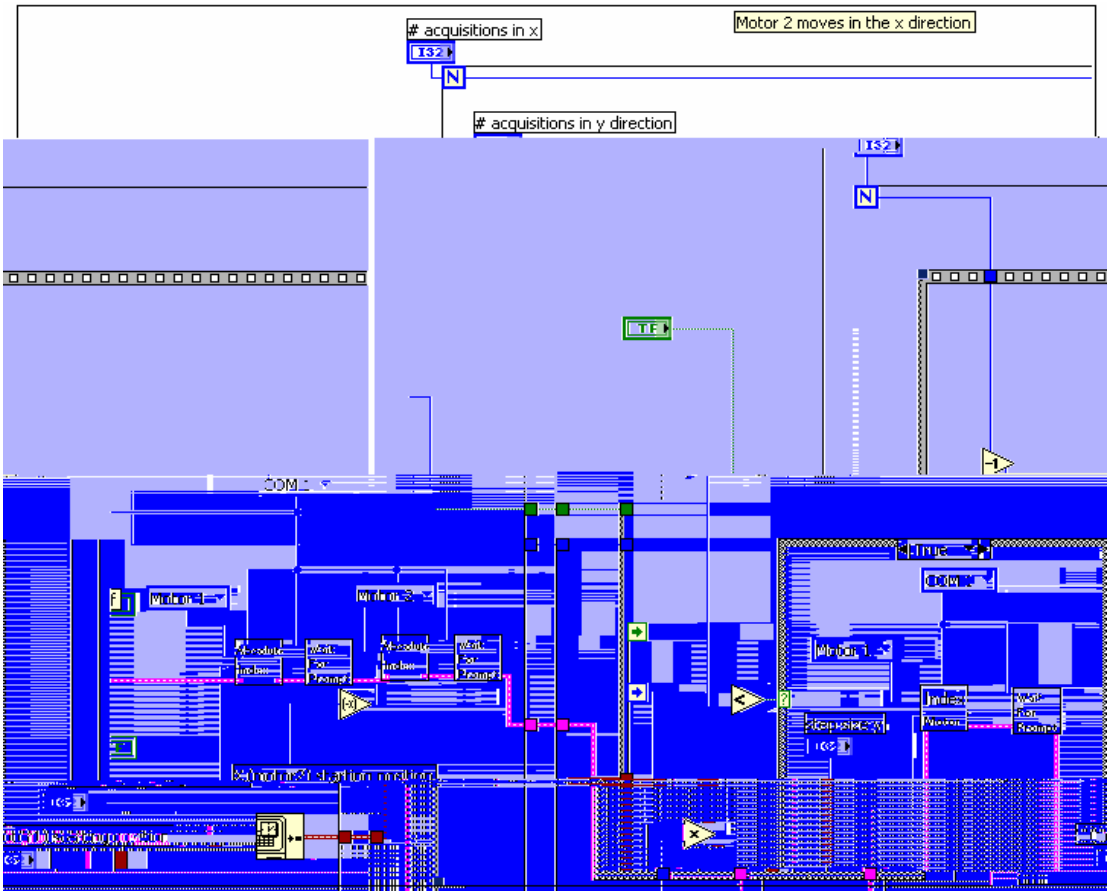

Figure A.3. Partial view of another loop of the spatial resolution block diagram. The Index Motor box within the loop takes values from user input controls and moves the translation stage motors to the desired positions.

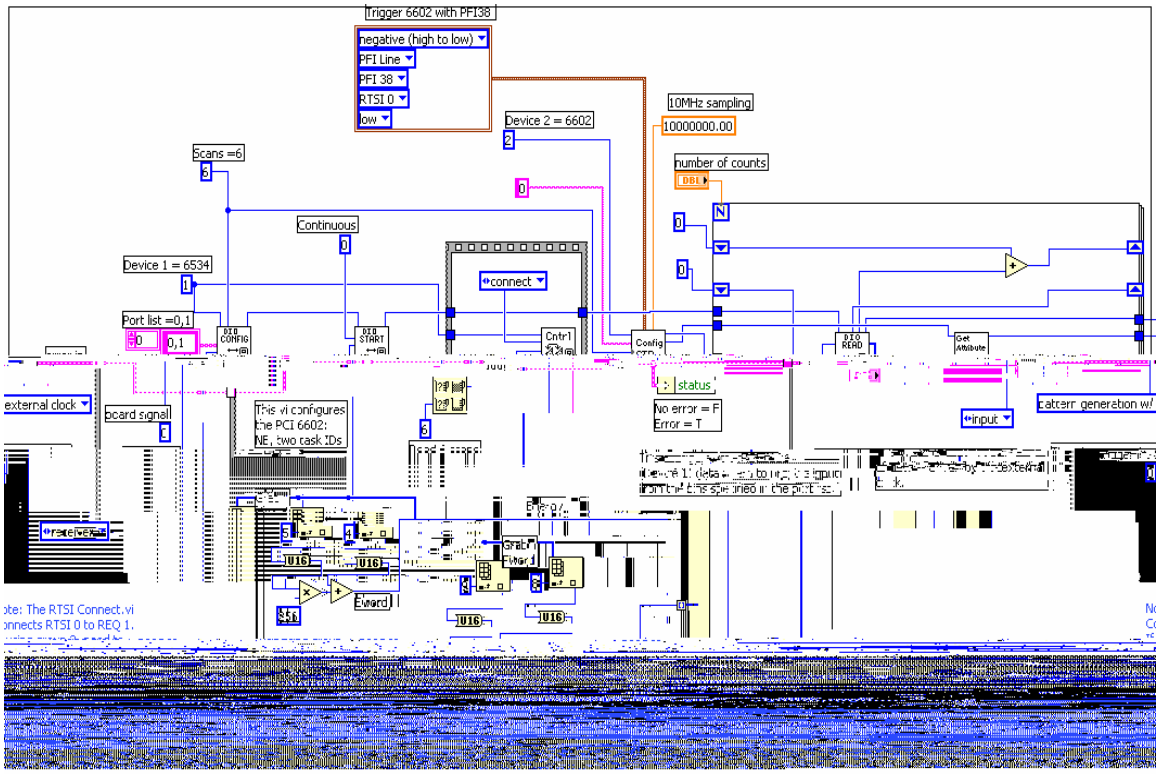

Figure B.2. Events2Disk block diagram.

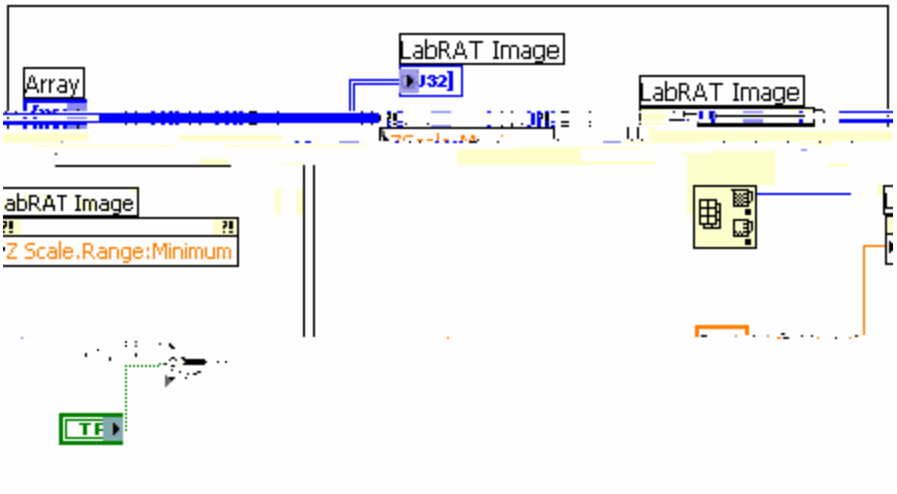

Figure B.3. Image display block diagram.

Appendix C

Detector Initialization Parameters

he had worked on there complete with the same initialization software and input files that we had started with. After an extensive analysis o2999i0c0]rsisanainput

the bad connection and results in this pixel having such a higher number of events than the rest of the module that all other pixels are washed out and the entire energy spectrum is dominated by this

f) ASIC thresh hold: This parameter is a finer voltage adjustment, sets thresh hold for individual ASICs. This is added or subtracted to the DFE thresh hold.

The other parameters in the input file are the ASIC number, main bias, trigger width, trigger delay, shaping time, preamp feedback, analog out voltage reference. These other parameters were tested and seemed to have little effect on the output of the detector, therefore they have a default setting of zero and are always set to zero.

Vita

Laurie Kelly was born in Pennsylvania but does not remember anything about Pennsylvania. She has lived in Farwell and Paw Paw Michigan, Truckee California, Reno Nevada, New Orleans and Baton Rouge Louisiana, and will soon move to Memphis Tennessee. After graduating from high school she enjoyed three interesting and happy years traveling across the United States, supporting herself by selling jewelry and other crafts. She became disillusioned with government altruism after a stint as an Americorps volunteer. Other jobs she has held are fast food cashier, waitress, factory worker, construction worker, office worker, video store clerk, casino buffet hostess and maid as well as student and research assistant and will soon be employed as a medical physicist. She received her bachelors in physics from the University of New Orleans in December of 2002 and started work on her master's in medical physics at Louisiana State University the following month. She is the proud mother of a lovely seven year old daughter, Sophia Surreal Davis, who has been with her throughout her entire higher education journey.